Characteristics of drag due to streamwise inhomogeneous roughness

I K Suastika[a], M L Hakim[a], B Nugroho[b], A Nasirudin[a], I K A P Utama[a], J P Monty[b] and B Ganapathisubramani[c]

[a]Department of Naval Architecture, Institut Teknologi Sepuluh Nopember, Surabaya 60111, Indonesia
[b]Department of Mechanical Engineering, The University of Melbourne, Victoria 3010, Australia
[c]Department of Aeronautics and Astronautics, University of Southampton, Southampton SO17 1BJ, United Kingdom

ARTICLE INFO

Keywords:
Biofouling
Energy efficiency
Inhomogeneous roughness
RANS simulations
Similarity laws
Skin friction

Abstract

Characteristics of the skin friction due to streamwise inhomogeneous roughness are investigated by modelling it in a simplified manner using step changes in equivalent sand grain roughness height k_s, denoted as P (k_s = 81.25 μm), Q (k_s = 325.00 μm) and R (k_s = 568.75 μm). The selected k_s values represent the common ship-hull roughness, i.e., from light slime to about small calcareous fouling. RANS simulations are performed to study the friction characteristics of various rough surfaces formed by a trio-combination of P, Q and R roughnesses on flat plates with streamwise lengths of 30, 60, 120 and 240 m. The three combinations of roughnesses form either homogeneous (PPP, QQQ or RRR) or inhomogeneous (PQR, PRQ, QPR, etc.) rough walled turbulent boundary layer flow. A step change in roughness height results in a sudden change of the local skin friction coefficient in the form of overshoot or undershoot, followed by a relaxation where the inhomogeneous local skin friction is slowly returning to the homogeneous local one. The sequence of roughness arrangement in a streamwise inhomogeneous roughness pattern plays a key role in the resulting overall skin friction with value increasing in the following order: PQR < PRQ < QPR < QRP < RPQ < RQP. The similarity laws hold for both homogeneous and inhomogeneous rough surfaces.

1. Introduction

Shipping is one of the most important means of transportation in the world. Nearly 80% of world's cargo is transported using this mode of transportation (UNCTAD, 2017). Due to its size, the shipping industry consumes a large amount of energy and it is responsible for 2.2% of global CO_2 emissions in 2012 (Smith et al., 2014). The International Maritime Organization (IMO) reports that in the absence of pollution policies, carbon dioxide emissions from the international shipping industries may grow by a factor of 2 to 3 by 2050 (compared to the emissions in 2007) as a result of the growth in shipping activities (Buhaug et al., 2009). To address this issue, various energy saving policies are introduced, such as Energy Efficiency Design Index (EEDI) and Energy Efficiency Operational Indicator (EEOI). Since then, there have been plenty of efforts by the shipping industry to reduce energy usage, i.e., to use more efficient engines, better hull design, etc. Many of these efforts contribute towards lowering fuel consumption. However, the bulk of large ship's energy usage is to overcome skin friction drag. It is estimated that approximately 80–90% of the total drags experienced by a large ship such as VLCC (Very Large Crude Carrier) comes from the skin friction drag (Kodama et al., 2000; Molland et al., 2014). The already high contribution of skin friction drag is exacerbated by the issue of hull roughness, which is generally associated with either hull imperfection or biofoulings (Schultz, 2007; Lindholdt et al., 2015). Such a hull roughness leads to a significant increase in skin friction drag. For example, light calcareous tubeworm fouling can increase the ship friction resistance by 23 to 34% (Monty et al., 2016) while a heavily fouled ship hull can increase it by 80% (Schultz, 2007). This condition ultimately leads to an increase in fuel consumption and its associated CO_2 emissions (Schultz et al., 2011; Hakim et al., 2019).

Considering the effects of hull roughness towards the economy and environment, there have been many efforts to characterize and estimate the increase of skin friction drag due to hull roughness in the last three decades. These

ORCID(s): 0000-0001-7909-1598 (I.K. Suastika)

include in-situ measurements (Lewthwaite et al., 1985; Nugroho et al., 2018; Utama and Nugroho, 2018), laboratory experiments (Schultz, 2004; Monty et al., 2016; Demirel et al., 2017b; Nugroho et al., 2020) and numerical simulations (Demirel et al., 2014, 2017a; Song et al., 2019, 2020a,b; Andersson et al., 2020). Many of the well established works rely on the assumption of the universality of the log-law in the mean velocity profiles (Granville, 1958; Marusic et al., 2013), where the viscous-scaled mean velocity U^+ over a smooth wall is similar to the rough surface with an additional downward shift, referred to as roughness function ΔU^+ (Clauser, 1954; Hama, 1954). The viscous-scaled mean velocity U^+ is given as $U^+ = U/u_\tau$, where U is the mean velocity and $u_\tau = \sqrt{\tau_w/\rho}$ is the so-called friction velocity (τ_w is the wall shear stress and ρ is the fluid density). This downward shift in the mean velocity profile is an indication of the increase in skin friction drag and it is a function of the roughness Reynolds number $k^+ = u_\tau k/\nu$, where ν is the kinematic viscosity and k is the roughness height (Nikuradse, 1933; Granville, 1958; Cebeci and Cousteix, 2005; Flack et al., 2012, 2016). The most well-known early investigation on the change of mean velocity profile due to roughness is the experimental study utilizing closely packed graded-sand roughened pipes by Nikuradse (1933). This seminal experiment coined the definition of "equivalent sand grain roughness height" k_s, which can be thought of as a measure of the influence of surface roughness on a wall-bounded flow. Although both k_s and k units are in meter, k_s can only be measured by exposing a moving fluid above the surface roughness of interest (Nikuradse, 1933; Hama, 1954; Perry and Joubert, 1963; Perry et al., 1969). In several previous works, the terms k and k_s are often interchanged (i.e., k_s is defined as k or vice versa), hence it is important to exercise caution in determining roughness height. Previous studies have clearly shown that k_s is not equal to k. Typically, k_s can be represented as a multiple of k (where the multiple can be greater or less than 1 depending on the choice of k) (Raupach et al., 1991; Jiménez, 2004). To the best of our knowledge, the use of equivalent sand grain roughness height k_s is preferred to capture the effect of roughness on the flow and, therefore, we follow this convention.

Following the rapid development of Computational Fluid Dynamics (CFD) in the last 30 years, it is now possible to simulate rough walled turbulent flow with an acceptable accuracy. Demirel et al. (2014) performed a relatively accurate Reynolds-averaged Navier-Stokes (RANS) simulations by employing STAR-CCM+ CFD software to study the friction resistance of flat plates due to antifouling coatings. They employed a modified wall function model that is based on the experimental data of Schultz (2004). Demirel et al. (2017a) extended their 2014 study to predict the ship friction resistance due to marine coatings and biofouling, including its effects on the ship powering. In more recent CFD studies, Song et al. (2019) also looked at the effect of biofouling on the ship hydrodynamic characteristics. A comprehensive review and comparison of different methods to model ship hull roughness are given by Andersson et al. (2020). Apart from just looking at ship hull roughness, many modern CFD simulations are now capable to include roughness in propeller and turbine performance studies, which is generally caused by cavitation and/or biofouling (Song et al., 2020a,b). Despite the advancement of rough walled flow CFD studies, many of the reported literatures assume that the roughness distribution is homogeneous. In reality, ship hull roughnesses, particularly those that arise from biofouling, rarely exist in such a homogeneous manner. From personal correspondences with ship operators, the authors found that there are more biofouling at the stern of the ship than at the front side, which may be influenced by the shear stress imparted by the flow on the hull. Furthermore, there is also an issue of inhomogeneity in the hull surface roughness that is mostly caused by the patches of biofouling that remain attached from the previous dry-docking. Many ship operators do not remove such an inhomogeneity due to the high cost of re-floating process. These inhomogeneities may cause a further increase in drag penalty or it may even result in a drag decrease, due to flow instability, such as large-scale vortices, internal boundary layer, etc.

In the last few decades there have been plenty of studies that looked into roughness inhomogeneities, particularly in the influence of streamwise step change from rough wall to smooth wall or vice versa (Antonia and Luxton, 1971, 1972; Wood, 1982; Smits and Wood, 1985; Hanson and Ganapathisubramani, 2016; Li et al., 2019), spanwise inhomogeneity between rough and smooth wall (Wangsawijaya et al., 2018, 2019, 2020) and spanwise inhomogeneity between two different roughnesses (Vanderwell and Ganapathisubramani, 2015; Ba et al., 2018). Despite these studies, one roughness inhomogeneity study that is rarely visited is the streamwise step change between two different roughness heights or more. One of the first studies that looked into step change from two different roughness heights is from Pendergrass and Arya (1984) where they simulated boundary layers over rural and urban type environment using sanspray and block roughness. They reported a development of internal boundary layer and significant shear stress overshooting above the roughness change before it settles down to the new surface equilibrium further down stream. A similar trend is also reported by Cheng and Castro (2002) where they used staggered blocks for the smoother surface and two-dimensional rib bar for the rougher surface. Bou-Zeid et al. (2004) conducted Large Eddy Simulation (LES) on two different roughness types, alternating over multiple patches, to simulate atmospheric boundary layer (ABL)

over heterogeneous land surfaces to understand the relationship between blending layer height and characteristic surface length scales. They found that a streamwise inhomogeneity has a complex effect on the wall boundary layer interaction and the sudden change in roughness characteristics causes sharp changes in the mean velocity profiles.

Given that it is well established that ship hull roughness due to biofouling is inhomogeneous, it is important to model this inhomogeneity to determine its effect on the ship friction resistance. To gain insight into the underlying physical processes, it is helpful to first examine the effect of this inhomogeneity in a simplified manner, for example, by considering streamwise step changes over several different roughness height groups. If, for example, a ship hull has three different types of roughness along its streamwise length (each characterized by its own value of k_s), can we determine the drag penalty of this surface and its associated representative roughness height k_s? How different is this drag penalty compared to the usual assumption of homogeneous roughness (i.e., constant k_s along the entire hull)? The purpose of this study is to seek answers to these questions. Reynolds-averaged Navier-Stokes (RANS) calculations are performed with varying values of k_s along a flat plate to determine the effects of inhomogeneous roughness on the drag penalty of the surface. To the best of our knowledge, there have not been many studies that looked into such cases systematically.

2. CFD Modeling

A Reynolds-averaged Navier-Stokes (RANS) model, implemented in ANSYS Fluent (ANSYS, 2013, 2017), is used to solve the turbulent flow over the flat plate with different roughness height k_s and various boundary layer development/plate length L. The RANS governing equations consist of averaged continuity and momentum equations, which for an incompressible flow without body forces, are given using tensor notation as follows:

$$\frac{\partial U_i}{\partial x_i} = 0 \tag{1}$$

$$\frac{\partial U_i}{\partial t} + \frac{\partial (U_i U_j)}{\partial x_j} = -\frac{1}{\rho}\frac{\partial P}{\partial x_i} + \frac{\partial}{\partial x_j}\left[\nu\left(\frac{\partial U_i}{\partial x_j} + \frac{\partial U_j}{\partial x_i}\right)\right] - \frac{\partial(\overline{u_i' u_j'})}{\partial x_j} \tag{2}$$

where $i, j = 1, 2, 3$, U_i is the mean velocity component, P is the mean pressure, ρ is the fluid density, ν is the kinematic viscosity, u_i' is the fluctuating velocity component and $-\rho\overline{u_i' u_j'}$ is the Reynolds stresses (Ferziger and Peric, 2002; Cebeci et al., 2005). A turbulence model, which relates the Reynolds stresses to the mean flow properties, is specified to close the system of equations (1-2). For that purpose, a $k-\epsilon$ turbulence model is utilized in this study. The turbulence model is a two-equation model representing the transports of turbulence kinetic energy k and turbulence dissipation rate ϵ (Jones and Launders, 1972; Shih et al., 1995).

As noted in the previous section, the effects of roughness manifest in a downward shift of the mean velocity profile in the log-law region with an amount of ΔU^+, which is a function of the roughness Reynolds number k^+ or k_s^+. The roughness function model used in this study is that proposed by Cebeci and Bradshaw (1977) whose model follows Nikuradse's uniform sand-grain roughness data (Nikuradse, 1933). Therefore, the roughness height utilized in this study is referred to as equivalent sand-grain roughness height k_s. Different roughness geometries are usually expressed in terms of a reference roughness, for which the sand-grain roughness height k_s is commonly used. The relation between k_s and k follows by noting that the velocity shift in the fully rough regime can be expressed as $\Delta U^+ = (1/\kappa)\ln(k^+) + B$ (Cebeci and Cousteix, 2005) so that, for the same velocity shift ΔU^+, the ratio k_s/k is given as $k_s/k = \exp\left[\kappa\left(B - B_s\right)\right]$, where κ is the von Kármán constant, B is a constant obtained from experiments and the subscript s refers to sand-grain roughness. The generalized Cebeci and Bradshaw's roughness function model, $\Delta U^+ = \Delta U^+(k_s^+)$ with $k_s^+ = u_\tau k_s/\nu$, where u_τ is the friction velocity and ν is the kinematic viscosity, is given as follows:

$$\Delta U^+ = \begin{cases} 0, & k_s^+ \leqslant k_{s;smooth}^+ \\ \frac{1}{\kappa}\ln\left[A\left(\frac{k_s^+/k_{s;smooth}^+}{k_{s;rough}^+ - k_{s;smooth}^+}\right) + C_s k_s^+\right]^a, & k_{s;smooth}^+ < k_s^+ \leqslant k_{s;rough}^+ \\ \frac{1}{\kappa}\ln\left(A + C_s k_s^+\right), & k_s^+ > k_{s;rough}^+ \end{cases} \tag{3}$$

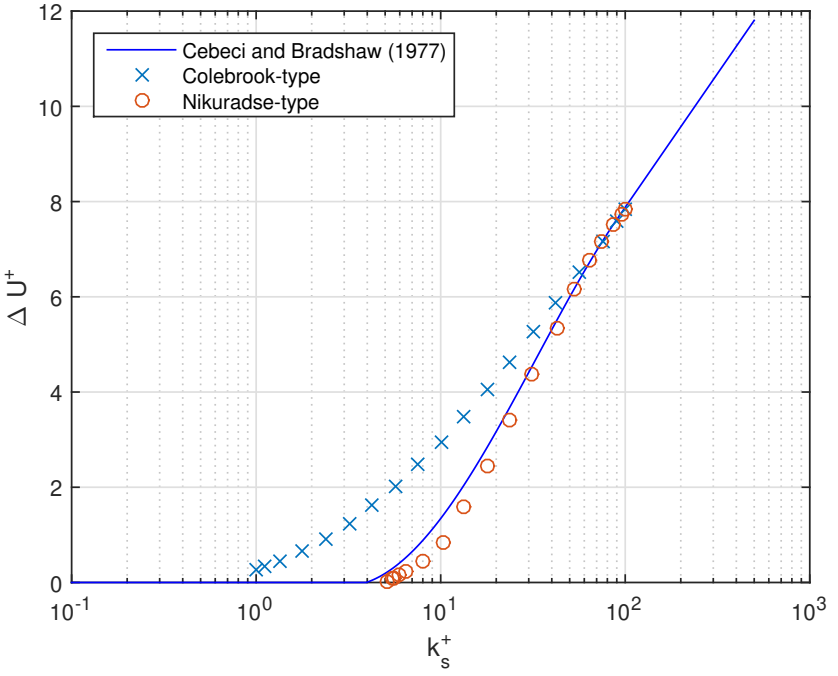

Figure 1: Cebeci and Bradshaw's roughness function (Cebeci and Bradshaw, 1977), which is based on Nikuradse's data (Nikuradse, 1933), compared with Colebrook's roughness data (Colebrook, 1939).

in which the power a is given as

$$a = \sin\left[\frac{\pi}{2}\frac{\log(k_s^+/k_{s;smooth}^+)}{\log(k_{s;rough}^+/k_{s;smooth}^+)}\right]$$

with $A = 0$, $k_{s;smooth}^+ = 2.25$, $k_{s;rough}^+ = 90.00$ and $C_s = 0.253$.

Determining the universal von Kármán constant κ has been an ongoing discussion in the last 60 years. Various reports show that it can vary between 0.35 and 0.42 (Foken, 2006; Hogstrom, 1988, 1996; Nagib and Chauhan, 2008; Marusic et al., 2013). The ANSYS Fluent software uses $\kappa = 0.41$. Equation (3) with $\kappa = 0.41$ (the same as the built in κ value in ANSYS Fluent) is plotted in Figure 1 together with Colebrook-type and Nikuradse-type roughness data (Colebrook, 1939; Nikuradse, 1933). The plot shows that Cebeci and Bradshaw's roughness function model follows Nikuradse-type sand grain roughness data well.

In the CFD modeling, the grid spacing near the wall is set to decrease exponentially as it moves normal towards the wall, as shown in Figure 2. A hexahedron-type mesh is chosen and it is arranged manually with an adjustable grid size. It is important to determine the mesh size near the wall to obtain an appropriate value for the dimensionless normal coordinate y^+, defined as $y^+ = u_\tau y/\nu$, where y is the outward wall normal coordinate, ν is the kinematic viscosity and u_τ is the friction velocity. The dimensionless variable y^+ is the Reynolds number based on the velocity scale u_τ and length scale y. To model the roughness effects correctly, the y^+ value for the first cell center above the wall must be larger than the local roughness Reynolds number k_s^+ (where $k_s^+ = u_\tau k_s/\nu$). To ensure this condition is always satisfied, ANSYS Fluent will virtually shift the wall if $y^+ < k_s^+$. For the roughness cases considered in this study, a blockage effect of 50% of the roughness height is assumed, and the corrected y^+ value for the first cell center above the wall is given as $y^+ = y^+ + k_s^+/2$. In this way the singularity issue is avoided and fine meshes can be handled correctly. The y^+ value for the first cell center above the wall targeted in the simulations is in the range $50 < y^+ < 254$ for smooth surfaces and in the order of 100 for rough surfaces. Verification and validation results regarding the y^+ value for the first cell center above the wall and the local roughness Reynolds number k_s^+ are presented in Section 4.

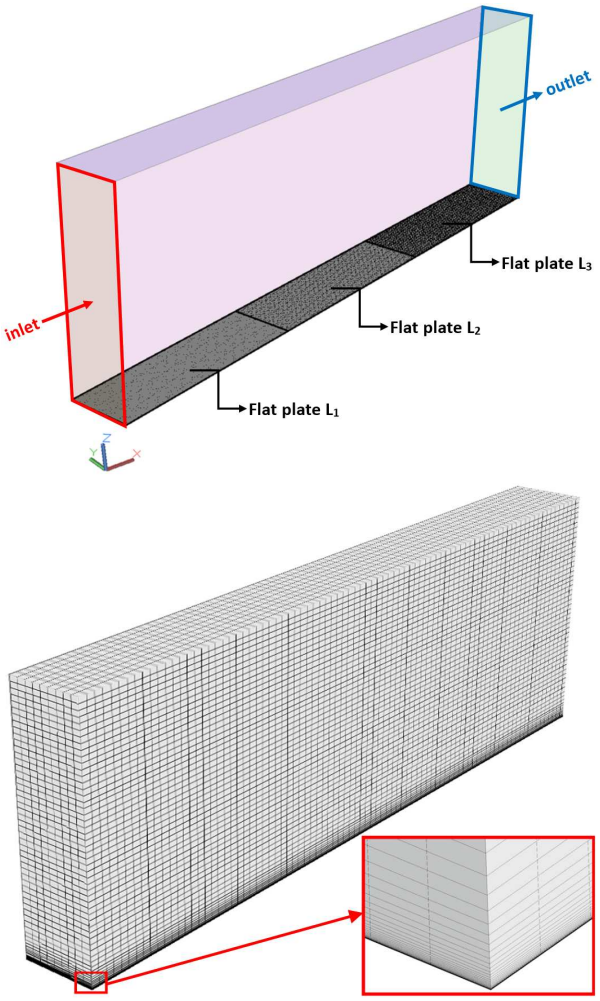

Figure 2: The top figure shows flow domain used in the simulations with three plate segments at the bottom boundary. On the inlet the flow velocity is prescribed by the free stream velocity $U_\infty = 9.77$ m/s (19 knots) while on the outlet the pressure is hydrostatic, ensuring no upstream propagation of disturbances (Mitchel et al., 2008). On the side and top boundaries, the boundary condition is free-slip while on the plate's surface it is no-slip. The lower figure shows a hexahedron mesh with an exponential cell height gradation near the wall bottom boundary.

Figure 2 illustrates the boundary conditions that we set for this study, where the inlet flow velocity is prescribed by the free stream velocity U_∞. To ensure there are no upstream propagation of disturbances, the outlet pressure is set to be hydrostatic (Mitchel et al., 2008). The no-slip condition is applied on the plate's surface while the top and side boundaries are modeled as free-slip walls. The boundary conditions, governing and turbulence modeling equations are discretized using a finite volume second-order method, resulting in a set of algebraic equations (Versteeg and Malalasekera, 2007; Moukalled et al., 2016). These set of algebraic equations are then solved using a finite volume solver, utilizing a SIMPLE algorithm in which gradient calculations are carried out using least-square cell-based method. The residual is set at 10^{-5} as convergence criterion. For all simulations in this study, the fluid properties and free stream velocity are kept constant. The fluid is seawater with mass density $\rho = 1025$ kg/m^3 and dynamic viscosity $\mu = 0.001077$ kg/(ms). Finally, the free stream velocity is set at $U_\infty = 9.77$ m/s (19 knots), which is a proper representative value of a typical ship speed.

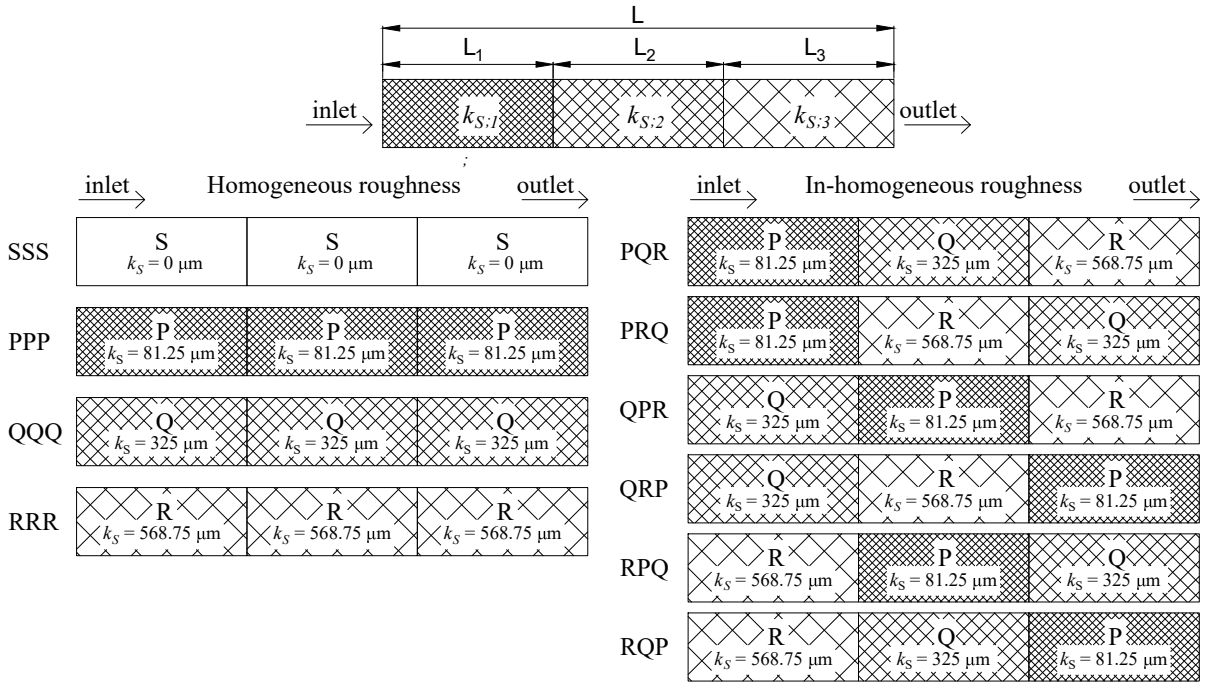

Figure 3: Combinations of three plate segments resulting in homogeneous (including fully smooth) and inhomogeneous rough surface conditions.

3. Surface Roughness Modeling

In this study we will look into two-parameter variations, namely the roughness height k_s and boundary layer development/plate length L. This section will explain details of the k_s and L set up and their possible combinations.

3.1. Roughness height variation

Four surface roughnesses with different k_s values are considered in this study, namely, smooth wall (S), small roughness height (P), medium roughness height (Q) and high roughness height (R) (see Table 1 for details). All three-combinations of roughnesses P, Q and R are considered to form either homogeneous or inhomogeneous rough walled turbulent boundary layer flow. For example, a three-surface combination of PPP, QQQ or RRR forms a homogeneous roughness while a combination of PQR, PRQ, QPR, etc. forms an inhomogeneous roughness. These k_s values are specifically chosen so that the average height of three different k_s of P (81.25 μm), Q (325.00 μm) and R (568.75 μm) will give an average height of Q, i.e., (81.25 μm + 325.00 μm + 568.75 μm)/3 = 325.00 μm. The selected k_s values are also designed to simulate the various stages of ship-hull biofouling growth, which range from light slime (Schultz, 2007) to about small calcareous fouling (Monty et al., 2016).

Table 1
Notations for the plate segments with their corresponding roughness heights k_s

Notation	S	P	Q	R
Sand-grain roughness height k_s [μm]	0.00	81.25	325.00	568.75

3.2. Boundary layer development/plate length variation

In addition to the variation of the sand grain roughness height, the total length of the plate L is also varied, where L = 30, 60, 120, and 240 m. These values of L are chosen because they are deemed representative for most ship lengths. Each of these L cases are divided into three equal lengths (L_1, L_2 and L_3), in which each represents a surface with a given roughness height (see Figure 3). The plate's width w in a simulation needs to be at least twelve times the thickness of the boundary layer that will be formed in the simulation. This would prevent any unwanted effects from the side walls. To estimate the necessary boundary layer thickness δ, we follow the results obtained by White (2011) representing δ for a smooth walled boundary layer flow as:

$$\delta = \frac{0.16x}{\mathrm{Re}^{1/7}} \tag{4}$$

where $\mathrm{Re} = \rho U_\infty x/\mu$ is the Reynolds number, ρ is the fluid density, U_∞ is the free stream velocity, x is the distance downstream from the start of the boundary layer (in this case, x is the plate length L) and μ is the dynamic viscosity. The calculated boundary layer thicknesses δ_s and δ_r, and chosen width w are tabulated in Table 2, where the subscripts s and r refer to smooth and rough surface, respectively. Some examples of case labeling for the different combinations of plate segments, forming homogeneous or inhomogeneous roughness pattern, including the fully smooth surface, are given in Table 3.

Table 2
Width of the plate calculated based on the turbulent boundary layer thickness δ ($\mathrm{Re} > 10^6$); subscripts s and r refer to smooth and rough, respectively.

Plate length L [m]	$\delta_s = \frac{0.16x}{\mathrm{Re}_x^{1/7}}$ [m]†	$\delta_r \approx 1.2\delta_s$ [m]	$12\delta_r$ [m]	Chosen width w [m]
30	0.298	0.358	4.30	5.0
60	0.540	0.649	7.78	8.0
120	0.979	1.17	14.10	15.0
240	1.77	2.13	25.54	26.0

† White (2011)

Table 3
Some examples of case labeling.

Case label	Roughness condition	L [m]	Roughness order
H30_SSS	Homogeneous	30	SSS
H60_PPP	Homogeneous	60	PPP
H120_QQQ	Homogeneous	120	QQQ
H240_RRR	Homogeneous	240	RRR
I30_PQR	Inhomogeneous	30	PQR
I60_QPR	Inhomogeneous	60	QPR
I120_RPQ	Inhomogeneous	120	RPQ
I240_RQP	Inhomogeneous	240	RQP

4. Verification and Validation of Modeling Results

4.1. Grid independence tests

To ensure that optimum number of cells are used in the final simulations, several grid independence tests using flat plate smooth wall base cases are conducted (H30_SSS, H60_SSS, H120_SSS and H240_SSS cases). For each case, the overall friction coefficient C_F is calculated using increasing number of cells in the simulation. The number of cells

in the latter simulation is approximately twice that in the former. The overall friction coefficient C_F is defined as

$$C_F = \frac{D}{\rho U_\infty^2 L/2} = \frac{\int_0^L \tau_w \mathrm{d}x}{\rho U_\infty^2 L/2} \tag{5}$$

where D is the drag per unit width, τ_w is the wall shear stress, ρ is the fluid density, U_∞ is the free stream velocity, L is the plate length and x is the distance downstream from the leading edge of the plate. Furthermore, a percent error $e_{n+1,n}$ between the lower and higher cell numbers is defined as follows:

$$e_{n+1,n} = \frac{C_F(n+1) - C_F(n)}{C_F(n)} \times 100\ [\%] \tag{6}$$

The results of the grid independence tests are summarized in Table 4. For the H30_SSS case, the number of cells are varied from 750,000 to 6,127,550. Table 4 shows that the value of C_F increases monotonically with increasing number of cells, which is expected to reach an asymptotic value at very large number of cells. The value of $e_{n+1,n}$ as listed in Table 4 decreases with increasing number of cells used in the simulation. The results show that the error is very low (in the range 0.0206 – 0.131% for the H30_SSS case), well below the recommended 2% from literature (see Anderson, 1995). Based on this grid independence test, $N = 3,000,000$ is chosen as an optimum number of cells for all the cases with $L = 30$ m (including homogeneous and inhomogeneous roughnesses). Similar tests are also conducted for the H60_SSS, H120_SSS and H240_SSS cases (longer plates). The results show that N = 3,318,200, 3,525,000 and 3,985,050 are the optimum numbers of cells for the cases with $L = 60$, 120 and 240 m, respectively.

Table 4
Frictional coefficients C_F calculated using increasing number of cells in the simulations for the smooth plate H30_SSS, H60_SSS, H120_SSS and H240_SSS cases.

Case	Run number n	Number of cells N	$C_F \times 10^3$	Percent error $e_{n+1,n}$ [%]
H30_SSS	1	750,000	1.7876	
	2	1,522,950	1.7899	0.131
	3	3,000,000	1.7905	0.0332
	4	6,127,550	1.7909	0.0206
H60_SSS	1	829,550	1.6395	
	2	1,675,000	1.6417	0.135
	3	3,318,200	1.6423	0.0400
	4	6,650,000	1.6428	0.0285
H120_SSS	1	776,600	1.5134	
	2	1,853,000	1.5153	0.121
	3	3,525,000	1.5159	0.0410
	4	6,779,500	1.5164	0.0308
H240_SSS	1	812,700	1.4082	
	2	1,950,000	1.4096	0.104
	3	3,985,050	1.4101	0.0353
	4	7,086,600	1.4105	0.0288

4.2. Verification and validation

In addition to the grid independence tests, further analyses are carried out for varied viscous-scaled wall normal distance y^+ ranges of the first cell center above the wall. For the smooth plate H30_SSS, H60_SSS, H120_SSS and H240_SSS cases, the calculation results are verified using the well-known Schoenherr's friction coefficient and the 1957 ITTC (International Towing Tank Conference) ship-model correlation line. The Schoenherr's friction coefficient C_F is given as:

$$\frac{0.242}{\sqrt{C_F}} = \log_{10}(\mathrm{Re}C_F) \tag{7}$$

It was adopted by ATTC (American Towing Tank Conference) as a standard for the clean hull skin friction resistance in 1947 and it is often referred to as the 1947 ATTC line. The second correlation is the 1957 ITTC ship-model correlation line, which is given as:

$$C_F = \frac{0.075}{\left[\log_{10}(\mathrm{Re}) - 2\right]^2} \tag{8}$$

In Equations (7–8) Re is the Reynolds number based on plate length (Re_L). A noticeable difference in C_F between Equations (7) and (8) is observed in the lower Reynolds number range ($\mathrm{Re} < 10^8$) where the ITTC 1957 formula gives larger values than the 1947 ATTC formula. At higher Re however, they are practically coincide with each other.

To quantify the accuracy of the CFD results, a percent error is defined between the CFD result and the 1947 ATTC line and, in a similar manner, between the CFD result and the 1957 ITTC ship-model correlation line. The percent error e in the latter case is calculated as follows:

$$e = \frac{C_{F;CFD} - C_{F;ITTC-1957}}{C_{F;ITTC-1957}} \times 100\ [\%] \tag{9}$$

The results are summarized in Table 5, showing C_F values calculated using different y^+ ranges for the first cell center above the wall targeted in the simulations.

Table 5
Overall friction coefficient C_F calculated using different ranges of y^+ value for the first cell center above the wall compared with 1947 ATTC (Equation 7) and 1957 ITTC (Equation 8) lines for the smooth H30_SSS, H60_SSS, H120_SSS and H240_SSS cases.

Case	Re_L	y^+ range		$C_F \times 10^3$			Percent error [%]	
		Min	Max	CFD	ATTC 1947	ITTC 1957	ATTC 1947	ITTC 1957
H30_SSS	2.79×10^8	64	112	1.7734	1.8017	1.8052	−1.57	−1.76
	2.79×10^8	155	254	1.7905	1.8017	1.8052	−0.620	−0.814
H60_SSS	5.58×10^8	74	126	1.6317	1.6468	1.6477	−0.921	−0.974
	5.58×10^8	149	249	1.6423	1.6468	1.6477	−0.273	−0.325
H120_SSS	1.12×10^9	88	142	1.5096	1.5104	1.5099	−0.0530	−0.0221
	1.12×10^9	144	235	1.5159	1.5104	1.5099	0.363	0.394
H240_SSS	2.23×10^9	86	133	1.4048	1.3897	1.3888	1.09	1.15
	2.23×10^9	140	227	1.4101	1.3897	1.3888	1.47	1.54

Table 5 shows that for the H30_SSS case, using a y^+ range between 155 and 254 would result in the closest C_F value to the 1947 ATTC and 1957 ITTC lines with percent errors of –0.620% and –0.814%, respectively. A smaller y^+ range will result in larger differences but the percentage differences do not exceed 1.76%, which is relatively small. A similar trend is also observed for the H60_SSS case. However, for the H120_SSS case, the shorter y^+ range of 88 and 142 results in the closest C_F value to the 1947 ATTC and 1957 ITTC lines with percent errors of –0.0530% and –0.0221%, respectively (lower error for the shorter y^+ range of 88 and 142). A similar trend of lower error for the shorter y^+ range is also observed on the H240_SSS case. Despite these anomalies, overall the percent errors between the CFD and the 1947 ATTC or the 1957 ATTC line are small. Table 5 also shows that, for the same value of Re_L, a larger y^+ value for the first cell center above the wall would result in a slightly larger C_F. Despite some discrepancies, for the smooth surface cases considered in this study, any y^+ range between 64 and 254 will result in an acceptable C_F value with maximum magnitude of percent errors of 1.57% when compared with the 1947 ATTC line and 1.76% when compared with the 1957 ITTC line. This result is in accordance with the recommended y^+ range in the literature for smooth flat plate CFD simulations, which is between 50 and 300 (Date and Turnock, 2000; Pope, 2000).

To model the roughness effects correctly, the y^+ value for the first cell center above the wall, denoted as $(\Delta y^+)_1$, must be larger than the local equivalent sand grain roughness Reynolds number k_s^+, i.e., $(\Delta y^+)_1 > k_s^+$. However, when one employs a fine mesh near the wall, the $(\Delta y^+)_1$ value may have a smaller value than the k_s^+ value, i.e., $(\Delta y^+)_1 < k_s^+$. If such a case happens, ANSYS Fluent applies a virtual shift of the wall by increasing the value of $(\Delta y^+)_1$ with an

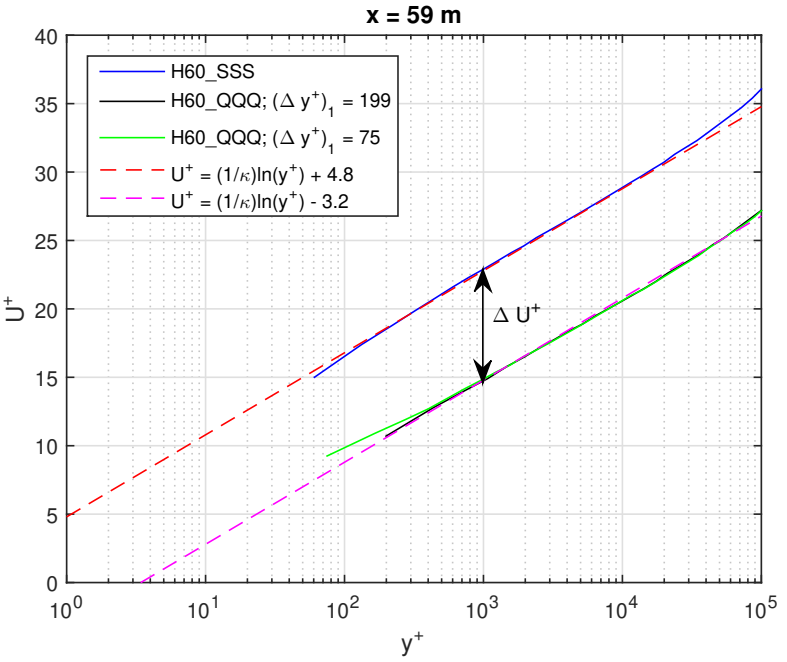

Figure 4: U^+ as function of y^+ for the homogeneous H60_QQQ case at $x = 59$ m ($\mathrm{Re}_x = 5.49 \times 10^8$) resulting from simulations with $(\Delta y^+)_1 = 199$ and $(\Delta y^+)_1 = 75$ compared with the reference smooth case H60_SSS. The downward shift of the velocity profile due to roughness effects is $\Delta U^+ \approx 8.0$ ($\kappa = 0.384$, $B_{1,s} = 4.8$).

amount $k_s^+/2$, such that $(\Delta y^+)_1 > k_s^+$. To illustrate this situation, Figure 4 shows results from the homogeneous roughness H60_QQQ as a test case. Figure 4 shows plots of mean velocity profiles U^+ as function of y^+ with two different values of $(\Delta y^+)_1$, namely $(\Delta y^+)_1 = 199$ (solid black line) and 75 (solid green line) obtained at the streamwise location near the plate's trailing edge ($x = 59$ m; with $\mathrm{Re}_x = 5.49 \times 10^8$). The velocity profile associated with the smooth wall surface is also shown in Figure 4 (solid blue line). At $y^+ > 400$ the two rough walled curves with different $(\Delta y^+)_1$ (solid black and green lines) coincide with each other, while at $y^+ < 400$ they are deviate. The roughness Reynolds number k_s^+ is calculated as $k_s^+ = u_\tau k_s/\nu$, where $u_\tau = \sqrt{\tau_w/\rho}$ and τ_w is obtained directly from the CFD simulation. The calculated value of τ_w for $(\Delta y^+)_1 = 75$ is 106.71 Pa resulting in $k_s^+ = 104.86$. On the other hand, the value of τ_w for $(\Delta y^+)_1 = 199$ is 106.53 Pa, which results in $k_s^+ = 104.77$ (less than 0.1% difference). The results show that although $(\Delta y^+)_1 < k_s^+$ (i.e., $(\Delta y^+)_1 = 75$ and $k_s^+ \approx 100$), the flow characteristics, indicated by the curve U^+ as function of y^+ and by the wall shear stress τ_w, are calculated correctly due to the application of a virtual shift of the wall method. In addition, the downward shift of the mean velocity profile ΔU^+ in the log-law region due to roughness effect is also shown in the figure, which is $\Delta U^+ \approx 8.0$ ($\kappa = 0.384$, $B_{1,s} = 4.8$).

As a mean for validating the CFD modeling results, we are calculating various ΔU^+, u_τ and k_s^+ values from the three homogeneous roughness cases (PPP, QQQ and RRR) at the streamwise locations $x = 29, 59, 119$ and 239 m, which correspond to Reynolds numbers $\mathrm{Re}_x = 2.70 \times 10^8, 5.49 \times 10^8, 1.11 \times 10^9$ and 2.22×10^9, respectively in a similar manner as illustrated in Figure 4. The resulting ΔU^+ and k_s^+ are then compared with the prescribed Cebeci and Bradshaw's roughness function (Equation 3). Figure 5 shows that the CFD results follow the prescribed roughness function well, indicating acceptable simulation results.

To gain more insight into the CFD results, they are verified using the analytical method of Granville (1958). Utilizing the similarity laws for the inner and outer layers of a turbulent boundary layer over a solid surface, the mean velocity profile in the overlap region (where the inner and outer laws are considered valid) is shown to have a logarithmic functional relationship (for both the smooth and rough surfaces). Based on the von Kármán momentum equation, a general logarithmic resistance formula can be obtained for a rough flat plate, which is applicable to quasi smooth, transitionally-rough and fully-rough regimes. The general logarithmic resistance formula represents the variation of overall friction coefficient C_F with Re_x for constant roughness Reynolds number k_s^+. This formula can be geometrically

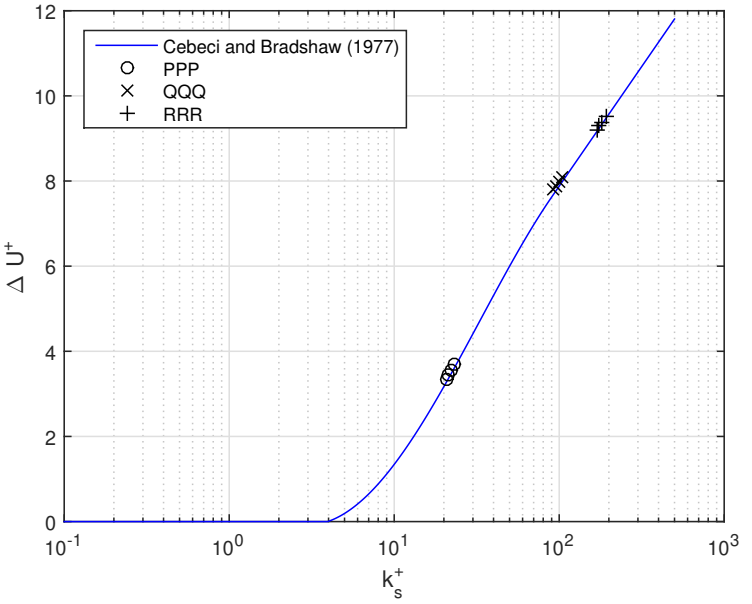

Figure 5: ΔU^+ as function of k_s^+ obtained from CFD simulations for homogeneous rough surfaces compared with the prescribed Cebeci and Bradshaw's roughness function. The roughness Reynolds number k_s^+ is calculated as $k_s^+ = u_\tau k_s/\nu$, where $u_\tau = \sqrt{\tau_w/\rho}$ for which τ_w resulted from CFD. The value of ΔU^+ isestimated in a similar way as illustrated in Figure 4, utilizing data of U^+ as function of y^+ at the corresponding locations.

interpreted as the shifting of the smooth surface curve (the 1947 ATTC line) horizontally in the $\log_{10}(\mathrm{Re}_x)$ direction to obtain a rough surface curve with constant k_s^+ (dashed lines in Figure 6). The shift is given by the following equation:

$$\log_{10}\left(\mathrm{Re}_x\right) - \log_{10}\left(\mathrm{Re}_{x,s}\right) = \frac{B_{1,s} - B_1}{2.3026A} \tag{10}$$

where the subscript s refers to the smooth surface curve. Subsequently, resistance lines of constant roughness ratio x/k_s can be obtained from the lines of constant k_s^+ by using the following relation:

$$\log_{10}\left(\mathrm{Re}_x\right) = \log_{10}\left(k_s^+\right) + \log_{10}\left(\frac{2}{C_F}\right)^{1/2} + \frac{A}{2.3026}\left(\frac{C_F}{2}\right)^{1/2} + \log_{10}\left(\frac{x}{k_s}\right) \tag{11}$$

Different values for the constant $B_{1,s}$ in Equation (10) are proposed and used in the literatures. For sand rough pipes, Nikuradse's data gives $B_{1,s} = 5.5$. For flat plates, Cebeci and Cousteix (2005) noted that $B_{1,s} \approx 5.0 - 5.2$ and used $B_{1,s} = 5.0$ in their modeling and computing of boundary-layer flows. Granville (1958), referring to Landweber (1953), listed $B_{1,s} = 4.0$, which fitted the 1947 ATTC line (Equation 7) best, and $2.3026A = 6$ or $A = 2.6058$ for the constant A. The constant A is related to κ as $A = 1/\kappa$, where κ is the von Kármán constant. The values of $B_{1,s} = 4.0$ and $\kappa = 1/A = 0.384$ listed by Granville (1958) are obtained from analysis of data of overall friction coefficients C_F. Results of analysis based on the overall friction coefficient C_F presented below with $A = 2.6058$ or $\kappa = 0.384$ indicate that $B_{1,s} \approx 4.0$ (see Figure 7), which is consistent with Granville's result. In addition, results of analysis based on the local wall shear stress τ_w as shown in Figure 4 indicate that $\kappa \approx 0.384$ and $B_{1,s} \approx 4.8$.

For a given roughness configuration, the quantity B_1 in Equation (10) is a function of the roughness Reynolds number k_s^+, i.e., $B_1 = B_1(k_s^+)$. The difference $B_{1,s} - B_1(k_s^+)$ is equal to $\Delta U^+(k_s^+)$, i.e., $B_{1,s} - B_1(k_s^+) = \Delta U^+(k_s^+)$, which is the roughness function. As discussed in Section 2, it is represented by Cebeci and Bradshaw's roughness function model in this study. The intersection of Equations (10) and (11) for given k_s^+ and x/k_s gives a point on the line of constant x/k_s at the specified k_s^+. This procedure, in combination with Cebeci and Bradshaw's roughness function given in Equation (3), is utilized in constructing the resistance diagrams shown in Figures 6 and 12.

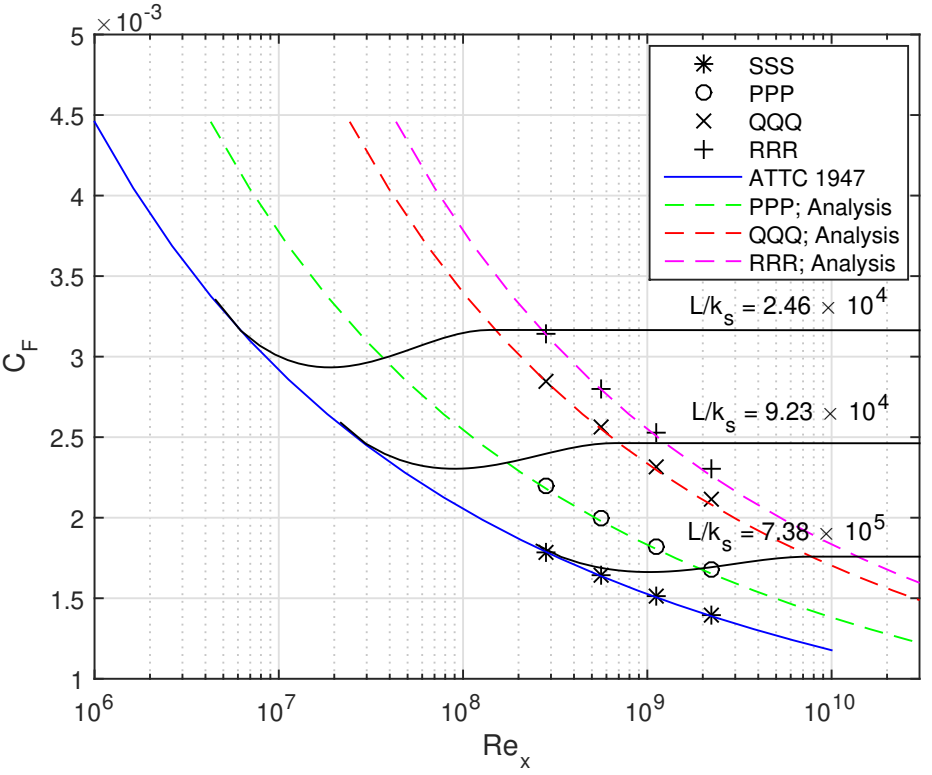

Figure 6: C_F as function of Re_x for constant values of roughness ratio L/k_s, obtained from Granville's analytical method (Granville, 1958) utilizing Cebeci and Bradshaw's roughness function given in Equation (3). The dashed lines are curves with constant k_s^+. Data are from CFD for smooth and homogeneous rough surfaces.

In addition, provided data of overall friction coefficient C_F as function of the Reynolds number Re_L, Granville (1958) gives an expression for the calculation of B_1 as follows:

$$B_1 = B_{1,s} - \frac{A}{2.3026}\frac{\mathrm{d}B_1}{\mathrm{d}\log_{10}(x^+)}\left(\frac{C_F}{2}\right)^{1/2} - 2.3026A\left[\log_{10}\left(\mathrm{Re}_x\right) - \log_{10}\left(\mathrm{Re}_{x,s}\right)\right] \tag{12}$$

The small effect due to $\mathrm{d}B_1/\left(\mathrm{d}\log_{10}x^+\right)$ in Equation (12) can be evaluated by iteration. However, because the term involving $\mathrm{d}B_1/\left(\mathrm{d}\log_{10}x^+\right)$ in Equation (12) is much smaller than the other terms, it is neglected in this study for simplicity. Granville (1958) introduced the parameter $x^+ = u_\tau x/\nu$ for the purpose of resistance characterization in which the single parameter variation of B_1 with k_s^+ is replaced by a two-parameter variation of B_1 with x^+ and x/k_s. Provided data of overall friction coefficient C_F as function of Re_L, the value of x^+ is calculated as follows:

$$\log_{10}\left(x^+\right) = \log_{10}\left(\mathrm{Re}_x\right) + \log_{10}\left(\frac{C_F}{2}\right)^{1/2} - \frac{A}{2.3026}\left(\frac{C_F}{2}\right)^{1/2} \tag{13}$$

Figure 7 shows the results of a resistance characterization using Equation (13) based on data of overall friction coefficient C_F as function of Re_L, showing B_1 as functions of x^+ and roughness ratio L/k_s for the smooth (SSS) and homogeneous rough (PPP, QQQ and RRR) surfaces. For surfaces with the same roughness height k_s and different lengths of plate, plots of B_1 as a function of $\log_{10}\left(x^+\right)$ are represented by curves offset with a constant amount given by the logarithm of the ratio of the lengths of the plates, which is in this case equal to $\log_{10}(2)$. As shown in Figure 7, these curves can be collapsed to a single line by parallel shifts of the curves in the x^+ direction, indicating that the similarity laws hold. This means that the resistance characteristic of a homogeneous rough surface but different lengths

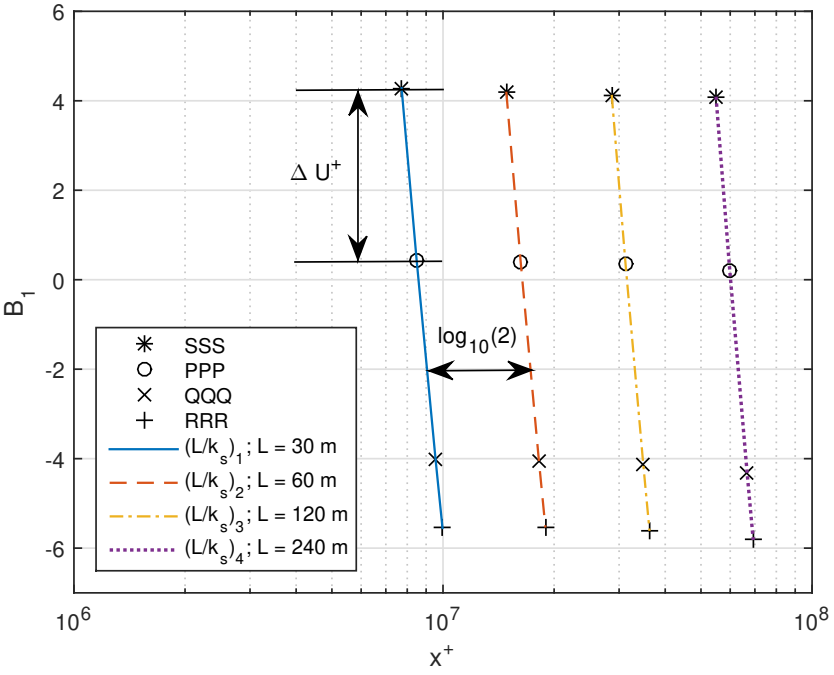

Figure 7: B_1 as function of $x^+ = u_\tau x/\nu$ and L/k_s, obtained from data of C_F as function of Re_L, following Granville's method (Granville, 1958) for the smooth and homogeneous rough surfaces. ΔU^+ is indicated for the H30_PPP case.

of plate is similar, which is characterized by the roughness height k_s. It is interesting to note that the observed values of $\Delta U^+ = B_{1,s} - B_1$ for surfaces with the same roughness height k_s but different lengths of plate are approximately the same. This is consistent with the observation that they lay on the same curve with constant k_s^+ (dashed lines in Figure 6 for the PPP, QQQ and RRR cases). Thus, based on Granville's analytical method utilizing data of overall friction coefficient C_F as function of Re_L, surfaces with the same roughness height k_s but different lengths of plate have the same overall ΔU^+ and k_s^+ values.

Finally, the mean values of ΔU^+ from plate lengths $L = 30, 60, 120$ and 240 m are 3.83, 8.30 and 9.81 for the PPP, QQQ and RRR cases, respectively, which indicate that the P roughness is in the transitionally rough regime while the R roughness is in the fully rough regime. The Q roughness sits at the start of the fully rough regime (see Figure 5). This discussion demonstrates that the CFD method provides consistent and accurate results for the purpose of skin friction calculations of smooth and homogeneous rough surfaces. It provides a reliable tool to explore the skin friction characteristics of inhomogeneous rough surfaces to be discussed in the following section.

5. Results and Discussion

A systematic analysis of the results from the inhomogeneous rough surface cases is given in this section. To study the roughness effects, the local (c_f) and overall (C_F) skin friction coefficients are calculated for both the homogeneous and inhomogeneous roughness cases. The effects from the roughness height and the roughness sequences in the streamwise direction are studied by analyzing the plots of local skin friction coefficient as a function of Reynolds number, and by comparing its integral values (C_F) for the different cases. We also calculate the skin friction coefficient percentage differences between rough surfaces (both homogeneous and inhomogeneous) and the smooth wall reference case, and between inhomogeneous roughness cases (combination of PQR) and the homogeneous roughness reference case (i.e., QQQ).

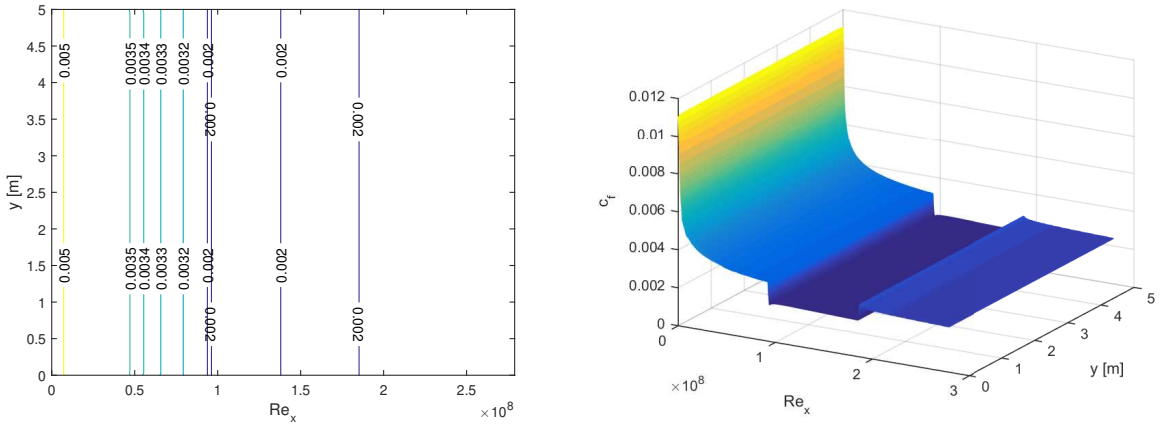

Figure 8: Contour (left) and 3D view (right) of the local skin friction coefficient c_f as function of the local Reynolds number Re_x and lateral position y for the inhomogeneous I30_RPQ case, showing practically no variation of c_f in the lateral direction.

5.1. Local skin friction c_f

The local skin friction coefficient c_f is defined as:

$$c_f = \frac{\tau_w}{\rho U_\infty^2/2} \tag{14}$$

where τ_w is the wall shear stress (obtained from CFD simulation), ρ is the fluid density and U_∞ is the free stream velocity. Simulation results show that the local skin friction coefficients c_f are uniform in the spanwise/lateral direction y (no variation of c_f in the spanwise/lateral direction) as intended (see Section 2 for the setting of the boundary conditions and Subsection 3.2 for the choice of plate width). To illustrate this, Figure 8 shows contour and 3D view of c_f as function of the local Reynolds number Re_x and lateral position y for the inhomogeneous I30_RPQ case. As shown in Figure 8, the c_f values are independent of y and it is only a function of Re_x. Figures 9 and 10 show c_f as a function of Re_x for the cases with plate lengths $L = 30$ and 240 m, respectively. Similar plots are also obtained for plate lengths $L = 60$ and 120 m but for brevity they are not shown here. Results from the shortest ($L = 30$ m) and longest ($L = 240$ m) plates are presented to underscore the effects of plate length on the resulting local skin friction coefficient. In both figures, the inhomogeneous PQR, PRQ, QPR, QRP, RPQ and RQP cases are compared with the homogeneous SSS, PPP, QQQ and RRR cases.

5.1.1. Homogeneous and inhomogeneous roughness

Figure 9 shows that the rough-wall homogeneous cases have a higher c_f than that of the smooth wall case at the same Re_x. This indicates that a rough wall surface indeed deviate from the smooth wall case and increases skin friction drag (Nikuradse, 1933). Within the homogeneous rough wall cases, the plots show that the highest k_s case (RRR) has a higher c_f value than those of the lower k_s cases (Q and P respectively) at equal Re_x. Such behaviour shows that a rougher surface will experience an elevated wall drag compared with less rough surfaces. The four homogeneous cases (including the smooth wall case) show a similar monotonic decrease in c_f with increasing Re_x. This classical result of exponential decrease of c_f with Re_x illustrates large friction near the leading edge of the plate (low Reynolds numbers), which decreases exponentially towards the trailing edge. Similar behaviour has been reported in various experimental and numerical studies (Monty et al., 2016; Demirel et al., 2017b; Pullin et al., 2017).

For the inhomogeneous cases with step changes in the equivalent sand grain roughness height k_s (PQR, PRQ, QPR, QRP, RPQ and RQP), the c_f values show step responses following the step change in k_s. For example, Figure 9a with PQR step changes case, show an increase in c_f every time there is an increase from P to Q and from Q to R height (P with $k_s = 81.25$ µm, Q with $k_s = 325.00$ µm, and R with $k_s = 568.75$ µm). Figure 9a shows that in the first one third part of the inhomogeneous rough plate ($0 < \mathrm{Re}_x < 0.9 \times 10^8$) with k_s value of 81.25 mm (P), the inhomogeneous case line

(magenta solid line) collapses with the homogeneous PPP case (red dotted line) well. However, as the inhomogeneous case arrives at the start of the second one third part of the plate ($0.9 \times 10^8 < \mathrm{Re}_x < 1.8 \times 10^8$), where it has k_s value of 325.00 μm (Q), the magenta line slightly jumps over (overshoot) the homogeneous QQQ case that is represented with an orange dashed-dotted line, and then the magenta line gradually fall down onto the homogeneous QQQ case. Finally, the last one third part of the inhomogeneous rough plate ($1.8 \times 10^8 < \mathrm{Re}_x < 2.7 \times 10^8$) has k_s value of 568.75 μm (R), and the plot clearly shows that the magenta line slightly overshoots the homogeneous RRR case (dashed black line) in the first few Re_x and then gradually collapses to the homogeneous RRR case. A similar behaviour is observed for all of the other five inhomogeneous roughness combinations (Figure 9b-f). The same features as shown in Figure 9 are also observed in Figure 10 for plate length $L = 240$ m but with smaller magnitudes of overshoot and undershoot.

Such a jump in c_f values between one surface profile to another surface profile has been reported by Andreopoulos and Wood (1982), where they measured the response of a smooth wall boundary layer to a perturbation/disturbance caused by a short sand-paper strip. The measured τ_w behind the strip was around three times the undisturbed value (fully smooth case). The sudden jump in c_f is followed by a relaxation, where the c_f is slowly returning to the smooth wall value. The relaxation rate was found to be very slow and Andreopoulos and Wood (1982) were unable to record any full recovery, even at the last measuring point. As observed by Andreopoulos and Wood (1982), our CFD results of local c_f shown in Figures 9 and 10 also exhibit a slow relaxation rate. However, RANS is unable to pick up the small-scale turbulence structures near the wall that occur at the border between the two roughness zones, which may actually influence the flow downstream. The wall model is not able to capture the flow physics fully but it provides us with some indications on the effect. Figures 9 and 10 indicate that the c_f value of the inhomogeneous rough surface will recover the underlying homogeneous rough wall c_f further downstream if the distance is sufficiently long. To quantify this, an averaged overshoot/undershoot will be defined and calculated in the following sub-subsection (5.1.2).

The overshoot and undershoot in skin friction are also observed in the seminal studies of Antonia and Luxton (1971, 1972) and discussed in other studies (Wood, 1982; Smits and Wood, 1985; Hanson and Ganapathisubramani, 2016; Li et al., 2019). It is argued that these happen naturally because of a change in the local Reynolds number and a sudden change in the relative roughness height. For smooth-to-rough cases (or generally step changes to a higher k_s), the step change results in a formation of a new internal boundary layer. Therefore, there is a large momentum flux away from the wall as the surface adapts to this condition before relaxing to the equilibrium with the new surface. The opposite condition is true for the rough-to-smooth transition (or generally step changes to a lower k_s). In addition, such a jump in the local skin friction coefficient c_f (or wall shear stress τ_w) in a turbulent flow is closely related to the mixing up behaviour of the plate at the leading edge. For example, when the flow travels from R to Q or from Q to P, the turbulent intensity of the flow is already high, so it does not require more mixing up and it reduces the turbulent intensity and eventually the Reynolds stress in the fluid and an undershoot occurs. The opposite takes place in a step-up jump. RANS is not able to capture all these phenomena and direct numerical simulations (DNS) may offer a remedy.

5.1.2. Overshoot and undershoot percentage differences

The overshoot and undershoot height of the flow seems to be based on the k_s of the following roughness. For example, when we look into the cases PQR and PRQ in the first row of Figure 9 (Figures 9a and b), the jump from P to Q is lower than that from P to R, resulting in a lower overshoot from P to Q than that from P to R. This also leads to a faster settling time for the P to Q jump than that for P to R case. Such behavior happens because R corresponds to a much higher k_s value than that corresponds to the Q case. Such undershoot and overshoot raise a question regarding how much is the difference in c_f between the homogeneous and inhomogeneous cases. To answer such a question, a percent error $e_{i,h}$ is defined between the areas under the c_f curves for the inhomogeneous and homogeneous cases as follows:

$$e_{i,h} = \frac{\int (c_{f;i} - c_{f;h}) \mathrm{dRe}_x}{\int c_{f;h} \mathrm{dRe}_x} \times 100\ [\%] \tag{15}$$

where the subscripts h and i refer to homogeneous and inhomogeneous case, respectively. The integral boundaries and the surface roughnesses for the homogeneous and inhomogeneous cases correspond to each other. For example, $e_{i,h}$

for the inhomogeneous case QPR is calculated as follows:

$$e_{i,h} = \frac{\int_0^{L_1}(c_{f;\mathrm{QPR}} - c_{f;\mathrm{QQQ}})\mathrm{dRe}_x + \int_{L1}^{L_1+L_2}(c_{f;\mathrm{QPR}} - c_{f;\mathrm{PPP}})\mathrm{dRe}_x + \int_{L_1+L2}^{L_2+L_3}(c_{f;\mathrm{QPR}} - c_{f;\mathrm{RRR}})\mathrm{dRe}_x}{\int_0^{L1} c_{f;\mathrm{QQQ}}\mathrm{dRe}_x + \int_{L_1}^{L_1+L_2} c_{f;\mathrm{PPP}}\mathrm{dRe}_x + \int_{L_1+L_2}^{L_2+L_3} c_{f;\mathrm{RRR}}\mathrm{dRe}_x} \times 100\,[\%] \quad (16)$$

Equation (16) shows that if the boundary layer responded to the step change instantly and there is no overshoot/undershoot from the homogeneous roughness curve, $e_{i,h}$ would be zero. A positive value of $e_{i,h}$ means that on average there is an overshoot while a negative value of $e_{i,h}$ means that there is an undershoot relative to the corresponding homogeneous curves. The values of $e_{i,h}$ are tabulated in Table 6.

Table 6 shows cases with decreasing magnitude of overshoot in the following order: PQR > PRQ > QPR and cases with decreasing magnitude of undershoot in the following order: RQP > RPQ > QRP. A consistent trend is observed in all the cases with different plate lengths. The largest averaged overshoot (1.87%) and undershoot (1.14%) are observed for plate length $L = 30$ m (I30_PQR and I30_RQP, respectively), followed subsequently by plate lengths $L = 60$, 120 and 240 m, with the lowest averaged overshoot of 0.160% (I240_QPR) and lowest averaged undershoot of 0.281% (I240_QRP). The magnitude of $e_{i,h}$ decreases with increasing plate length for surfaces with the same roughness configuration. This indicates that, following the overshoot/undershoot, the c_f value of the inhomogeneous rough surface will recover the underlying homogeneous rough wall c_f further downstream if the distance is sufficiently long.

5.2. Overall skin friction C_F

Following the local skin friction analysis from the previous section, it is desirable to estimate the overall skin friction coefficient C_F of the plates. This allows us to see the influence of individual roughness height k_s or the combination of it in a more global way. The overall skin friction coefficient C_F is given in Equation (5). It is related to the local skin friction coefficient $c_f(x)$ by the following relation:

$$C_F = \frac{\int_0^L c_f(x)\mathrm{d}x}{L} \quad (17)$$

The corresponding overall skin friction coefficients C_F's for the plate segments 1, 2 and 3 are given, respectively, as follows:

$$C_{F;1} = \frac{\int_0^{L_1} c_f(x)\mathrm{d}x}{L_1}; \quad C_{F;2} = \frac{\int_{L_1}^{L_1+L_2} c_f(x)\mathrm{d}x}{L_2}; \quad C_{F;3} = \frac{\int_{L_1+L_2}^{L_2+L_3} c_f(x)\mathrm{d}x}{L_3} \quad (18)$$

where x is the distance in the streamwise direction with the origin at the leading edge of the plate. The lengths of plate segments 1, 2 and 3 are denoted as L_1, L_2 and L_3, respectively. Table 6 summarizes the overall C_F and those for each plate segments ($C_{F;1}$, $C_{F;2}$, $C_{F;3}$).

Table 6 shows that for the homogeneous cases, both the smooth SSS and the three rough cases (PPP, QQQ and RRR), the overall friction coefficient C_F decreases as the flow moves from the upstream to downstream ($C_{F;1} > C_{F;2} > C_{F;3}$). These results are consistent with the observations of the local friction coefficient c_f discussed above, that is, lower c_f as Re_x increases. The RRR case has the largest C_F among the three homogeneous roughness cases for the same Re_L due to its highest k_s value. For an increasing Re_L, the C_F for shorter plate is larger than that of the longer plate for the same roughness height, for example, H30_RRR > H60_RRR > H120_RRR > H240_RRR.

The inhomogeneous case C_F distribution however, is not as straight forward as the homogeneous case due to the combination of Reynolds number, roughness height and step jump. Consider first the cases with plate length $L = 30$ m. When one looks at Table 6, cases I30_PQR and I30_PRQ, it is clear that the first plate section overall coefficients ($C_{F;1}$) for both I30_PQR and I30_PRQ have the same C_F value of 2.607×10^{-3} due to the same k_s value (both are P cases). However, when we look at $C_{F;2}$ from I30_PQR and $C_{F;3}$ from I30_PRQ (both correspond to Q case), it is clear that they have different individual C_F values. The $C_{F;2}$ from I30_PQR is 2.736×10^{-3} while the $C_{F;3}$ from I30_PRQ is 2.473×10^{-3}. An explanation for this observation is as follows. First, it should be noted that PQR is a step change from P to Q [akin to the smooth-rough case of Antonia and Luxton (1971, 1972)] while PRQ is a step change from R to Q [similar to the rough-smooth case of Antonia and Luxton (1971, 1972)]. Because of the different nature of the step

changes with overshoot in the former case and undershoot in the latter case, the local c_f of the inhomogeneous case does not overlay on the c_f value of the homogeneous Q case. Second, there is a nonlinear relationship between c_f and the local Reynolds number Re_x, where c_f decreases exponentially with increasing Re_x. These result in different overall C_F values for any inhomogeneous (PQR) combinations. The inhomogeneous C_F values increase in the following order: PQR < PRQ < QPR < QRP < RPQ < RQP. A similar trend is observed for all the inhomogeneous cases with longer plate lengths, $L = 60, 120$ and 240 m (larger Reynolds numbers).

Table 6
Overall friction coefficients for the plate segments $C_{F;1}, C_{F;2}, C_{F;3}$ and the entire plate C_F, and the percent errors $e_{r,s}, e_{i,q}$ and $e_{i,h}$

		Overall friction coefficient						
Case	Re_L	$C_{F;1} \times 10^3$	$C_{F;2} \times 10^3$	$C_{F;3} \times 10^3$	$C_F \times 10^3$	$e_{r,s}$ [%]	$e_{i,q}$ [%]	$e_{i,h}$ [%]
H30_SSS	2.79×10^8	2.075	1.700	1.596	1.791	0.00		
H30_PPP	2.79×10^8	2.608	2.062	1.915	2.195	22.60		
H30_QQQ	2.79×10^8	3.436	2.660	2.454	2.850	59.19	0.00	
H30_RRR	2.79×10^8	3.809	2.918	2.685	3.137	75.23		
I30_PQR	2.79×10^8	2.607	2.736	2.759	2.700	50.82	−5.26	1.87
I30_PRQ	2.79×10^8	2.607	3.037	2.473	2.706	51.12	−5.07	1.71
I30_QPR	2.79×10^8	3.437	2.007	2.770	2.738	52.92	−3.94	0.371
I30_QRP	2.79×10^8	3.436	2.951	1.846	2.745	53.29	−3.71	−0.439
I30_RPQ	2.79×10^8	3.811	1.988	2.484	2.761	54.21	−3.13	−0.518
I30_RQP	2.79×10^8	3.810	2.633	1.846	2.763	54.32	−3.06	−1.14
H60_SSS	5.58×10^8	1.885	1.566	1.476	1.642	0.00		
H60_PPP	5.58×10^8	2.351	1.882	1.758	1.997	21.62		
H60_QQQ	5.58×10^8	3.053	2.398	2.228	2.559	55.84	0.00	
H60_RRR	5.58×10^8	3.362	2.615	2.424	2.800	70.51		
I60_PQR	5.58×10^8	2.351	2.460	2.482	2.431	48.02	−5.02	1.68
I60_PRQ	5.58×10^8	2.351	2.711	2.243	2.435	48.25	−4.87	1.53
I60_QPR	5.58×10^8	3.054	1.837	2.492	2.461	49.84	−3.85	0.313
I60_QRP	5.58×10^8	3.053	2.641	1.701	2.465	50.10	−3.68	−0.426
I60_RPQ	5.58×10^8	3.363	1.821	2.252	2.479	50.93	−3.15	−0.477
I60_RQP	5.58×10^8	3.362	2.376	1.701	2.480	50.99	−3.11	−1.04
H120_SSS	1.12×10^9	1.723	1.450	1.375	1.516	0.00		
H120_PPP	1.12×10^9	2.112	1.723	1.621	1.819	19.97		
H120_QQQ	1.12×10^9	2.718	2.180	2.043	2.314	52.62	0.00	
H120_RRR	1.12×10^9	2.981	2.370	2.217	2.523	66.41		
I120_PQR	1.12×10^9	2.112	2.230	2.263	2.202	45.23	−4.84	1.47
I120_PRQ	1.12×10^9	2.112	2.447	2.055	2.205	45.43	−4.71	1.36
I120_QPR	1.12×10^9	2.719	1.686	2.270	2.225	46.77	−3.83	0.245
I120_QRP	1.12×10^9	2.718	2.391	1.576	2.228	46.99	−3.69	−0.369
I120_RPQ	1.12×10^9	2.981	1.673	2.062	2.239	47.68	−3.23	−0.441
I120_RQP	1.12×10^9	2.981	2.162	1.576	2.240	47.74	−3.20	−0.921
H240_SSS	2.23×10^9	1.584	1.353	1.293	1.410	0.00		
H240_PPP	2.23×10^9	1.914	1.592	1.513	1.673	18.65		
H240_QQQ	2.23×10^9	2.444	2.005	1.902	2.117	50.12	0.00	
H240_RRR	2.23×10^9	2.669	2.176	2.062	2.302	63.25		
I240_PQR	2.23×10^9	1.914	2.044	2.094	2.017	43.06	−4.70	1.19
I240_PRQ	2.23×10^9	1.914	2.234	1.911	2.020	43.23	−4.59	1.13
I240_QPR	2.23×10^9	2.444	1.564	2.100	2.036	44.37	−3.83	0.160
I240_QRP	2.23×10^9	2.444	2.191	1.481	2.038	44.56	−3.70	−0.281
I240_RPQ	2.23×10^9	2.669	1.554	1.916	2.047	45.13	−3.32	−0.381
I240_RQP	2.23×10^9	2.669	1.992	1.481	2.047	45.18	−3.29	−0.740

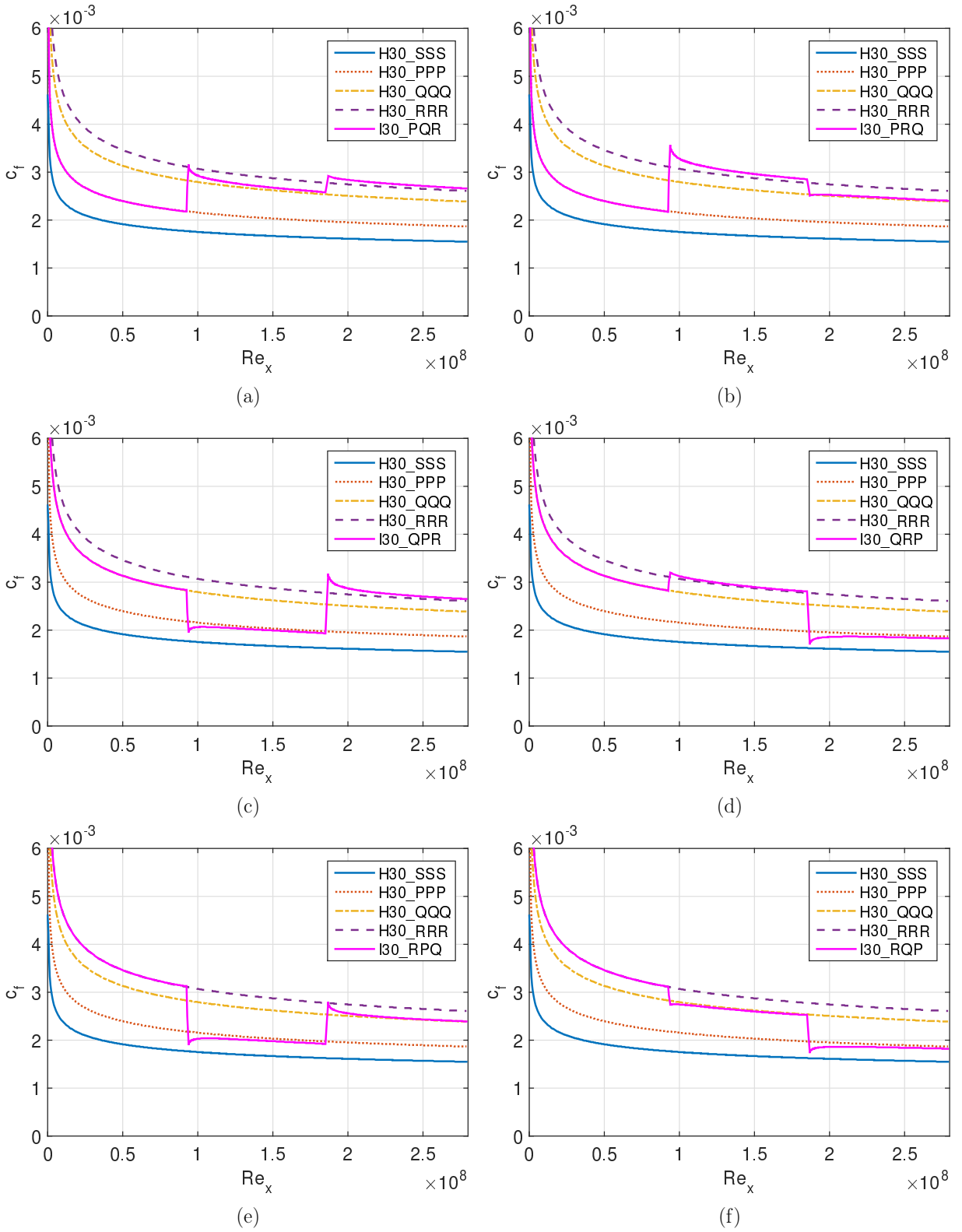

Figure 9: Coefficient of local skin friction $c_f = \tau_w / \left(\rho U_\infty^2/2\right)$ as function of the local Reynolds number Re_x for the inhomogeneous PQR, PRQ, QPR, QRP, RPQ and RQP cases compared with the homogeneous SSS, PPP, QQQ and RRR cases (plate length $L = 30$ m).

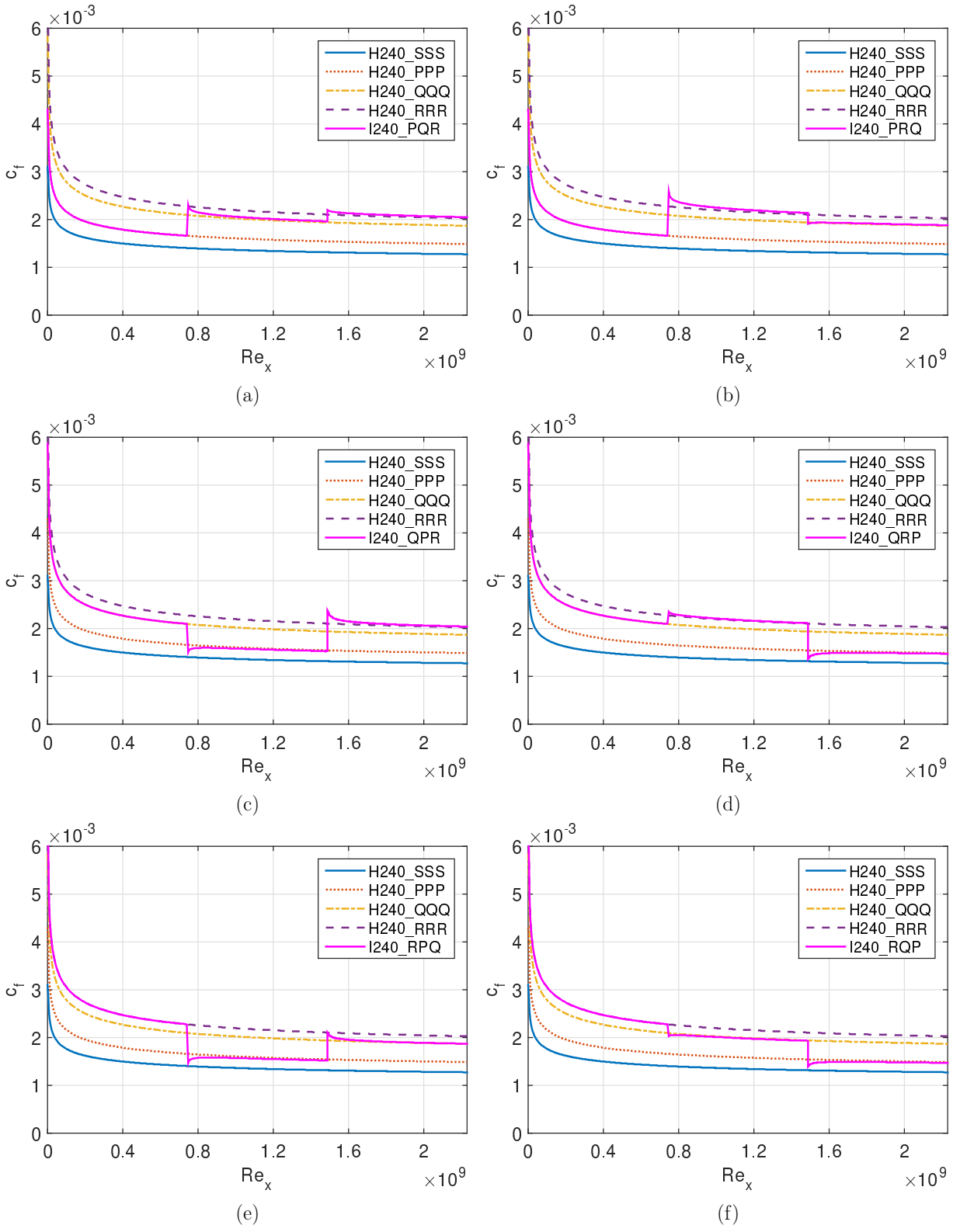

Figure 10: Coefficient of local skin friction $c_f = \tau_w / \left(\rho U_\infty^2/2\right)$ as function of the local Reynolds number Re_x for the inhomogeneous PQR, PRQ, QPR, QRP, RPQ and RQP cases compared with the homogeneous SSS, PPP, QQQ and RRR cases (plate length $L = 240$ m).

5.2.1. Quantification of the overall skin friction between rough surface and smooth surface

Having obtained the overall skin friction C_F from individual plates, allows us to quantify the change in drag penalty between one case to another in a more simplified way. The first analysis that we are interested to do is to quantify the roughness wall effects (both homegenous and inhomogeneous cases) on the overall skin friction relative to the smooth wall case. A percent increase in overall skin friction $e_{r,s}$ due to roughness effects is defined as follows:

$$e_{r,s} = \frac{C_{F;r} - C_{F;s}}{C_{F;s}} \times 100\ [\%] \tag{19}$$

The subscripts r and s refer to rough and smooth, respectively. The results are tabulated in Table 6.

Table 6 shows that the H30_RRR case results in the highest $e_{r,s}$ due to the reasons explained above (shortest plate and highest k_s) with a value of 75.23%. For the same reasons, the smallest $e_{r,s}$ resulted from the H240_PPP case, with a value of 18.65%. It is interesting to note that the homogeneous H120_QQQ case with $k_s = 325$ µm experienced an increase in drag penalty of 52.62% compared to the smooth wall case. Such a value of roughness height represents heavy slime (Schultz, 2007) or fouled with light calcareous tube-worm fouling (Monty et al., 2016). This 52.62% drag penalty is very close to the experiment of Monty et al. (2016) where similar k_s and Reynolds number (tube worm on a 124 m operating ship, running at 9 m/s, which is close to the cruise speed) resulted in a drag increase of 49% with respect to the smooth wall case.

A similar rough and smooth wall $e_{r,s}$ analysis is also conducted for the inhomogeneous cases. The results show that the homogenous QQQ case (with $k_s = 325$ µm) for the same Reynolds number has a higher percent increase in overall skin friction $e_{r,s}$ than the inhomogeneous cases. Although the averaged roughness heights for the inhomogeneous cases are the same as the QQQ roughnes height, their representative roughness heights are smaller than the QQQ roughness height and depend on the sequence of roughness heights in the streamwise direction. It is observed that the values of $e_{r,s}$ for the inhomogeneous cases increase monotonically in the following order: PQR < PRQ < QPR < QRP < RPQ < RQP. The corresponding representative k_s are expected to increase in the same order (to be quantified in Subsection 5.3). Clearly, the sequence of roughness height plays a crucial role to result in this behaviour. When the first plate is set to be the highest k_s value (R) and then followed by the mid (Q) and lowest (P) sequentially, it will result in a higher $e_{r,s}$ than any other combinations. On the other hand, the PQR configuration, starting from the lowest (P) to the highest (R) k_s, will result in the lowest $e_{r,s}$ value.

5.2.2. Quantification of the overall skin friction between inhomogeneous and homogeneous rough surface

Apart from looking at the percent increase in overall skin friction $e_{r,s}$ between rough wall and smooth wall, it is also desirable to quantify the effects of roughness inhomogeneity (combination of PQR) on the overall skin friction C_F with respect to the homogeneous QQQ baseline case. For that purpose, a percent decrease between an inhomogeneous roughness case and the homogeneous QQQ case is defined as follows:

$$e_{i,q} = \frac{C_{F;i} - C_{F;\mathrm{QQQ}}}{C_{F;\mathrm{QQQ}}} \times 100\ [\%] \tag{20}$$

The subscript i refers to inhomogeneous roughness (variation of PQR) while the subscript QQQ refers to the homogenous rough wall base case. As has been noted above, the friction coefficient $C_{F;\mathrm{QQQ}}$ is chosen as a reference because the arithmetic average of k_s for the inhomogeneous cases is equal to that of the homogeneous QQQ case. Calculating skin friction from measured surface roughness would normally use a single roughness value which generally comes from the average of measurements over the hull (Molland et al., 2011). Thus, $e_{i,q}$ represents the error of assuming a single (average) roughness value for an inhomogeneously rough hull. A negative value of $e_{i,q}$ indicates that the C_F values of the inhomogeneous cases (combination of PQR) are lower than the homogeneous base case (QQQ). The opposite is true for a positive value of $e_{i,q}$. Table 6 shows that the $e_{i,q}$ values are negative for all the inhomogeneous cases, indicating that the C_F values of all the inhomogeneous cases (combination of PQR) are lower than the homogeneous base case (QQQ). For the same plate length, the magnitude of $e_{i,q}$ decreases orderly in sequence of PQR to RQP, indicating that the order of roughness arrangement plays a key role. This behaviour is observed in all plate length (Reynolds number) cases. For the cases under consideration, the maximum percentage difference is 5.26% for the I30_PQR case.

There are two possible reasons for a difference between the inhomogeneous cases and the homogeneous (QQQ)

case. The first is that there is a nonlinear relationship between c_f and the local Reynolds number as shown in Figures 9 and 10. This means that a change to the roughness near the leading edge (low Re) has fractionally larger contribution to the friction coefficient change compared with a change to the roughness further downstream. It is therefore critical that the location of the measured roughness is known for accurate calculation of the drag. Figures 9 and 10 are useful in visually explaining this behaviour. These figures show the contribution to C_F for each segment of the inhomogeneous roughened plates for the cases with $L = 30$ and 240 m. The second reason is that a step change in roughness causes a complex response from the boundary layer such that the skin friction overshoots/undershoots before decaying back to the homogeneous rough wall curve as discussed in Subsection 5.1.

It is clear that for the inhomogeneous cases, the order of placement of the roughness is important, that is, a different order of placement results in a different value of C_F. Although the difference is relatively small, Table 6 shows that the RQP case results in the highest C_F while the PQR case results in the smallest. This result can be understood in view of the above-mentioned nonlinearity of the c_f curve with local Reynolds number. The higher roughness (R) at the front for the RQP case, where $C_{F;1}$ is much higher than that of the PQR case, outweighs the negative effect of a lower roughness (P) at the back, where $C_{F;3}$ is lower. This is expected to be always true for inhomogeneous rough surfaces, no matter the choice of roughness magnitude. In practical terms, limiting (cleaning) the biofouling from the bow of the vessel is of greatest benefit and should be prioritized.

5.3. Prediction of a representative roughness height for an inhomogeneous rough surface

Having discussed the local and overall skin frictions in Subsections 5.1 and 5.2, a question may arise: "Can we predict a representative roughness height k_s for an inhomogeneous rough surface?" To answer such a question, the data of C_F as function of Re_L presented in Subsection 5.2 will be utilized along with Granville's analytical method discussed in Section 4.

Utilizing the data of overall friction coefficient C_F as function of Re_L presented in Subsection 5.2, a resistance characterization is carried out using Equation (13). Figure 11 shows that the resistance characteristics of the inhomogeneous rough surfaces, represented by plots of B_1 as functions of x^+ and L/k_s, follow the same curves as for the homogeneous rough surfaces discussed in Section 4. Therefore, similar to the homogeneous rough surfaces, the similarity laws also hold for the inhomogeneous rough surfaces. This means that, for example, the resistance characteristics of the I30_PQR, I60_PQR, I120_PQR and I240_PQR roughnesses are similar, and they can be represented by a single roughness height k_s. For the same reason, it is also true for all of the other inhomogeneous rough surfaces. As for the homogeneous rough surfaces discussed in Section 4, it is interesting to note that (inhomogeneous rough) surfaces with the same roughness configuration but different lengths of plate lay on the same curve with constant overall k_s^+ (dashed lines in Figure 12) and that they have approximately the same value of overall ΔU^+ (see Figure 11).

The mean values of ΔU^+ from plate lengths $L = 30, 60, 120$ and 240 m are 7.41, 7.44, 7.61, 7.64, 7.73 and 7.74 for the inhomogeneous rough PQR, PRQ, QPR, QRP, RPQ and RQP surfaces, respectively, indicating that they are in the transitionally rough regime (see Figures 5 and 12). Because they are in the transitionally rough regime, the general logarithmic formula given in Equation (11) can be utilized for the purpose of roughness height prediction, because it is is applicable to quasi smooth, transitionally-rough and fully-rough regimes. The procedure is as follows: given a value of ΔU^+ (for which the mean value is used), the value of k_s^+ is calculated using Cebeci and Bradshaw's roughness function given in Equation (3). For the known k_s^+, C_F and Re_L values, the value of L/k_s can be calculated from Equation (11). Finally, for the known L/k_s and L, the value of k_s is determined. The roughness heights k_s for the homogeneous rough surfaces are also calculated for the purpose of verification of prediction results. The results are summarized in Table 7.

Table 7 shows that the differences between given and predicted values of k_s for the homogeneous rough surfaces are relatively small with a maximum magnitude of percent error of 1.74%, indicating sufficiently accurate prediction results within 5% error. The predicted k_s values for the inhomogeneous rough surfaces increase in the following order: PQR < PRQ < QPR < QRP < RPQ < RQP and they are smaller than the k_s value of the homogeneous QQQ case. These results are consistent with those presented in Subsection 5.2.

6. Conclusions

Wall bounded roughness flow is a complex physical phenomenon which results in the increase of skin friction drag. Because the surface roughness of a ship hull fouled with biofoulings or other type of hull imperfections is often found to be inhomogenous, it is important to consider inhomogenous roughness in addition to homogeneous roughness. In this

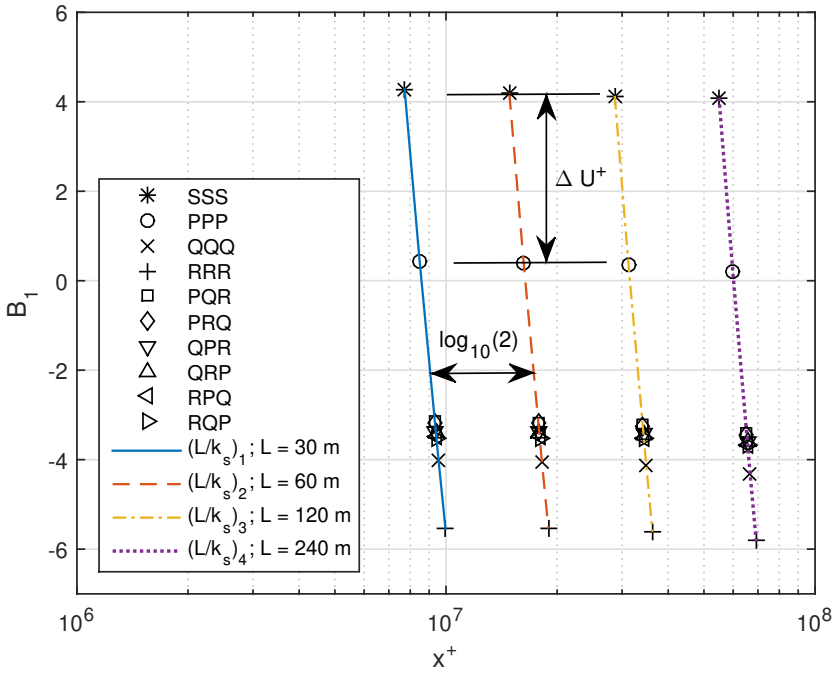

Figure 11: B_1 as function of $x^+ = u_\tau x/\nu$ and L/k_s, obtained from data of C_F as function of Re_L, following Granville's method (Granville, 1958) for all cases including the smooth, homogeneous and inhomogeneous rough surfaces. ΔU^+ is indicated for the H60_PPP case.

Table 7
Prediction of roughness height k_s for homogeneous and inhomogeneous rough surfaces. Subscripts p and g refer to predicted and given values, respectively.

Roughness configuration	ΔU^+	k_s^+	$k_{s;p}$ [μm]	$k_{s;g}$ [μm]	Percent error $e_{p,g}$ [%]
PPP	3.83	21.77	82.11	81.25	1.06
QQQ	8.30	98.10	330.65	325.00	1.74
RRR	9.81	174.36	564.50	568.75	−0.747
PQR	7.41	69.24	238.83		
PRQ	7.44	69.96	241.13		
QPR	7.61	74.18	254.54		
QRP	7.64	74.97	257.07		
RPQ	7.73	77.39	264.74		
RQP	7.74	77.67	265.65		

study, the effects of roughness inhomogeneity on the skin friction drag are investigated by modeling the inhomogeneous roughness pattern in a simplified manner using step changes in the equivalent sand grain roughness heights k_s, denoted as P, Q and R.

Such a step change in the roughness height results in an overshoot/undershoot of the local skin friction coefficient c_f, followed by a relaxation where the c_f value is slowly returning to the underlying rough wall homogeneous c_f value. A step up in k_s results in an overshoot while a step down in k_s causes an undershoot in the c_f values. In some cases where the jump happens over two significantly different k_s values (i.e., P to R), the relaxation rate is found to be very slow and it is unable to fully recover over the given stream wise distance. Cases with decreasing magnitude of overshoot are found in the following order: PQR > PRQ > QPR, and cases with decreasing magnitude of undershoot are in the following order: RQP > RPQ > QRP. The largest averaged overshoot (1.87%) and undershoot (1.14%) are

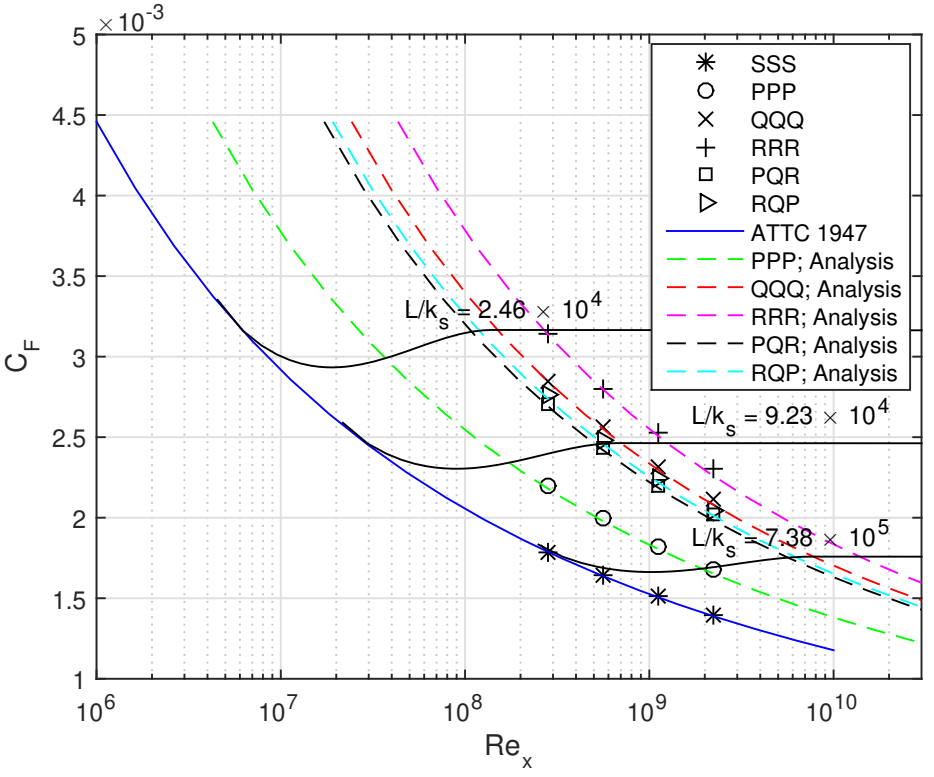

Figure 12: C_F as function of Re_x for constant values of roughness ratio L/k. Dashed lines are curves with constant k_s^+. Data are from CFD for smooth, homogeneous and inhomogeneous rough surfaces. Only the PQR and RQP roughnesses are shown for the inhomogeneous rough surfaces for brevity.

from the shortest plate (I30_PQR and I30_RQP, respectively), followed subsequently by longer plates with the lowest averaged overshoot of 0.160% (I240_QPR) and lowest averaged undershoot of 0.281% (I240_QRP). For surfaces with the same roughness configuration but different lengths of plate, the averaged overshoot/undershoot decreases with increasing plate length, indicating that, following the overshoot/undershoot, the inhomogeneous rough c_f will recover the underlying homogeneous rough wall c_f further downstream if the distance is sufficiently long.

The sequence of roughness arrangement in a streamwise inhomogeneous roughness pattern plays a key role in the resulting overall skin friction coefficient C_F. It is found that C_F increases in the following order: PQR < PRQ < QPR < QRP < RPQ < RQP. This result is further reflected in the predicted k_s values, showing k_s increases in the same order: PQR < PRQ < QPR < QRP < RPQ < RQP. A change of roughness near the leading edge of the plate has a much more significant effect on the overall skin friction coefficient C_F than a change of this near the trailing edge. In practical terms, limiting (cleaning) the biofouling from the bow of a ship is of greatest benefit and should be prioritized.

Finally, the similarity laws hold for both homogeneous and inhomogeneous rough surfaces; surfaces with the same roughness configuration but different lengths of plate have the same representative roughness height k_s.

Acknowledgments

This research project was supported by the Ministry of Research, Technology and Higher Education of the Republic of Indonesia under the World Class Professor 2019 Grant, in collaboration with the University of Melbourne, Australia, and the University of Southampton, UK, with Grant Contract No. T/42/D2.3/KK.04.05/2019. BG gratefully acknowledged the support from EPSRC (Grant Ref. No. EP/R034370/1).

References

Anderson, J.D., 1995. Computational Fluid Dynamics: The Basics with Applications. McGraw-Hill, Inc. doi:https://doi.org/10.1017/CBO9780511780066.

Andersson, J., Oliveira, D., Yeginbayeva, I., Leer-Andersen, M., Bensow, R., 2020. Review and comparison of methods to model ship hull roughness. Applied Ocean Research 99, 102–119. doi:https://doi.org/10.1016/j.apor.2020.102119.

Andreopoulos, J., Wood, D.H., 1982. The response of a turbulent boundary layer to a short length of surface roughness. J. Fluid Mech. 118, 143–164.

ANSYS, 2013. ANSYS Fluent Theory Guide, Release 15.0. ANSYS, Inc. doi:http://www.ansys.com.

ANSYS, 2017. ANSYS Help Viewer (Fluent) v.18.1. ANSYS, Inc. doi:http://www.ansys.com.

Antonia, R.A., Luxton, R.E., 1971. The response of turbulent boundary layer to a step change in surface roughness. part 1. smooth to rough. J. Fluid Mech. 48, 721–761.

Antonia, R.A., Luxton, R.E., 1972. The response of turbulent boundary layer to a step change in surface roughness. part 2. rough to smooth. J. Fluid Mech. 53, 737–757.

Ba, H.L., Kevin, Hutchins, N., Monty, J.P., 2018. Turbulence modifications in a turbulent boundary layer over a rough wall with spanwise-alternating roughness strips. Phys. Fluids 30, 055105. doi:https://doi.org/10.1063/1.5026134.

Bou-Zeid, E., Meneveau, C., Parlange, M.B., 2004. Large-eddy simulation of neutral atmospheric boundary layer flow over heterogeneous surfaces: Blending height and effective surface roughness. Water Resources Research 40(2), 1–18.

Buhaug, Ø., Corbett, J., Endresen, Ø., Eyring, V., Faber, J., Hanayama, S., Lee, D., Lindstad, H., Markowska, A., Mjelde, A., Nelissen, D., Nilsen, J., Palsson, C., Winebrake, J., Wu, W., Yoshida, K., 2009. Second IMO GHG Study. Technical Report. International Maritime Organization.

Cebeci, T., Bradshaw, P., 1977. Momentum transfer in boundary layers. Hemisphere Publishing Corporation, New York.

Cebeci, T., Cousteix, J., 2005. Modeling and Computation of Boundary-Layer Flows. Horizons Publishing, Long Beach, California and Springer, Heidelberg.

Cebeci, T., Shao, J., Kafyeke, F., Laurendeau, E., 2005. Computational Fluid Dynamics for Engineers. Horizons Publishing, Long Beach, California and Springer, Heidelberg.

Cheng, H., Castro, I.P., 2002. Near-wall flow development after a step change in surface roughness. Boundary-Layer Meteorology 105, 411–432. doi:https://doi.org/10.1023/A:1020355306788.

Clauser, F.H., 1954. The turbulent boundary layer in adverse pressure gradients. J. Aero. Sci. 21, 333–358.

Colebrook, C., 1939. Turbulent flow in pipes with particular reference to the transition region between the smooth and rough pipe laws. J. Inst. Civil Eng. 11, 133–156. doi:https://doi.org/10.1680/ijoti.1939.13150.

Date, J.C., Turnock, S.R., 2000. Computational fluid dynamics estimation of skin friction experienced by plane moving through water. Trans. Royal Inst. Naval Arch. 142, 116–135.

Demirel, Y.K., Khorasanchi, M., Turan, O., Incecik, A., Schultz, M.P., 2014. A cfd model for the frictional resistance prediction of antifouling coatings. Ocean Eng. 89, 21–31. doi:https://doi.org/10.1016/j.oceaneng.2014.07.017.

Demirel, Y.K., Turan, O., Incecik, A., 2017a. Predicting the effect of biofouling on ship resistance using cfd. Appl. Ocean Res. 62, 100–118. doi:https://doi.org/10.1016/j.apor.2016.12.003.

Demirel, Y.K., Uzun, D., Zhang, Y., Fang, H.C., Day, A.H., Turan, O., 2017b. Effect of barnacle fouling on ship resistance and powering. Biofouling 33, 819–834. doi:https://doi.org/10.1080/08927014.2017.1373279.

Ferziger, J.H., Peric, M., 2002. Computational Methods for Fluid Dynamics. Springer.

Flack, K.A., Schultz, M.P., Barros, J.M., Kim, Y.C., 2016. Skin-friction behavior in the transitionally-rough regime. Int. J. Heat Fluid Flow 61, 21–30. doi:https://doi.org/10.1016/j.ijheatfluidflow.2016.05.008.

Flack, K.A., Schultz, M.P., Rose, W.B., 2012. The onset of roughness effects in the transitionally rough regime. Int. J. Heat Fluid Flow 35, 160–167. doi:https://doi.org/10.1016/j.ijheatfluidflow.2012.02.003.

Foken, T., 2006. 50 years of the monin-obukhov similarity theory. Boundary-Layer Meteorology 119, 431–447.

Granville, P.S., 1958. The frictional resistance and turbulent boundary layer of rough surfaces. J. Ship Res. 2, 52–74.

Hakim, M.L., Nugroho, B., Nurrohman, M.N., Suastika, I.K., Utama, I.K.A.P., 2019. Investigation of fuel consumption on an operating ship due to biofouling growth and quality of anti-fouling coating, in: IOP Conf. Series: Earth and Environmental Sci. doi:https://doi.org/10.1088/1755-1315/339/1/012037.

Hama, F.R., 1954. Boundary-layer characteristics for smooth and rough surfaces. Trans. Soc. Nav. Archit. Mar. Engrs 62, 333–358.

Hanson, R.A., Ganapathisubramani, B., 2016. Development of turbulent boundary layers past a step change in wall roughness. J. Fluid Mech. 795, 494–523.

Hogstrom, U., 1988. Non-dimensional wind and temperature profiles in the atmospheric surface layer: a re-evaluation. Boundary-Layer Meteorology 42, 55–78.

Hogstrom, U., 1996. Review of some basic characteristics of the atmospheric surface layer. Boundary-Layer Meteorology 78, 215–246.

Jiménez, J., 2004. Turbulent flows over rough walls. Annu. Rev. Fluid Mech 36, 173–196.

Jones, W., Launders, B., 1972. The prediction of laminarization with a two-equation model of turbulence. Int. J. Heat and Mass Transfer 15, 301–314.

Kodama, Y., Kakugawa, A., Takahashi, T., Kawashima, H., 2000. Experimental study on microbubbles and their applicability to ships for skin friction reduction. Int. J. Heat Fluid Flow. 21, 582–588.

Landweber, L., 1953. The frictional resistance of flat plates in zero pressure gradient. Trans. SNAME 61.

Lewthwaite, J.C., Molland, A.F., Thomas, K.W., 1985. An investigation into the variation of ship skin frictional resistance with fouling. R. Inst. Naval. Architects. Trans. 127, 269–284.

Li, M., de Silva, C.M., Rouhi, A., Baidya, R., Chung, D., Marusic, I., Hutchins, N., 2019. Recovery of wall-shear stress to equilibrium flow conditions after a rough-to-smooth step change in turbulent boundary layers. J. Fluid Mech. 872, 472–491.

Lindholdt, A., Dam-Johansen, K., Olsen, S.M., Yebra, D.M., Kiil, S., 2015. Effects of biofouling development on drag forces of hull coatings for

ocean-going ships: a review. J. Coat. Technol. Res. 12(3), 415–444.
Marusic, I., Monty, J.P., Hultmark, M., Smits, A.J., 2013. On the logarithmic region in wall turbulence. J. Fluid Mech. 716, R3, 1–11.
Mitchel, R.R., Webb, M.B., Roetzel, J.N., Lu, F.K., Dutton, J.C., 2008. A study of the base pressure distribution of a slender body of square cross section, in: Proceeding of the 46th AIAA Aerospace Sciences Meeting and Exhibition, Reno, Nevada, pp. 1–8.
Molland, A.F., Turnock, S.R., Hudson, D.A., 2011. Ship Resistance and Propulsion. Cambridge University Press, New York, USA.
Molland, A.F., Turnock, S.R., Hudson, D.A., Utama, I.K.A.P., 2014. Reducing ship emissions: A review of potential practical improvements in the propulsive efficiency of future ships. Trans. Royal. Inst. Naval Archit. Part A: Int. J. Maritime Engineering 156, 175–188. doi:https://doi.org/10.3940/rina.ijme.2014.a2.289.
Monty, J.P., Dogan, E., Hanson, R., Scardino, A.J., Ganapathisubramani, B., Hutchins, N., 2016. An assessment of the ship drag penalty arising from light calcareous tubeworm fouling. Biofouling 32, 451–464. doi:https://doi.org/10.1080/08927014.2016.1148140.
Moukalled, F., Mangani, L., Darwish, M., 2016. The Finite Volume Method in Computational Fluid Dynamics. Springer, Switzerland.
Nagib, H., Chauhan, K., 2008. Variations of von kármán coefficient in canonical flows. Phys. Fluids. 20, 101518.
Nikuradse, J., 1933. Laws of flow in rough pipes (english translation of stromungsgesetze in rauhen rohren). Vdi-forschungsh. 361. Beilage zu "Forschung auf dem Gebiete des Ingenieurwesens" (Translation from NACA Tech. Memo. 1292) 361. doi:https://doi.org/10.1063/1.1715007.
Nugroho, B., Baidya, R., Nurrohman, M.N., Yusim, A.K., Prasetyo, F.A., Yusuf, M., Suastika, I.K., Utama, I.K.A.P., Monty, J.P., Hutchins, N., Ganapathisubramani, B., 2018. In-situ turbulent boundary layer measurements over freshly cleaned ship-hull under steady cruising, in: Proceeding of ICSOT: Development in Ships Design and Construction, Depok, Indonesia, pp. 43–48.
Nugroho, B., Monty, J.P., Utama, I.K.A.P., Ganapathisubramani, B., Hutchins, N., 2020. Non k-type behaviour of roughness when in-plane wavelength approaches the boundary layer thickness. J. Fluid Mech (in-press) doi:https://doi.org/10.1017/jfm.2020.875.
Pendergrass, W., Arya, S.P.S., 1984. Dispersion in neutral boundary layer over a step change in surface roughness - mean flow and turbulence structure. Atmos. Environ. 18, 1267–1279.
Perry, A.E., Joubert, P.N., 1963. Rough-wall boundary layers in adverse pressure gradients. J. Fluid Mech. 17, 193–211.
Perry, A.E., Schofield, W.H., Joubert, P.N., 1969. Rough wall turbulent boundary layers. J. Fluid Mech. 37, 383–413.
Pope, S., 2000. Turbulent Flows. Cambridge University Press.
Pullin, D.I., Hutchins, N., Chung, D., 2017. Turbulent flow over a long flat plate with uniform roughness. Phys. Rev. Fluids 2, 082601. doi:https://doi.org/10.1103/PhysRevFluids.2.082601.
Raupach, M.R., Antonia, R.A., Rajagopalan, S., 1991. Rough-wall turbulent boundary layers. Appl. Mech. Rev. 44, 1–25.
Schultz, M.P., 2004. Frictional resistance of antifouling coating systems. J. Fluids Eng. Trans. ASME 126, 1039–1047. doi:https://doi.org/10.1115/1.1845552.
Schultz, M.P., 2007. Effects of coating roughness and biofouling on ship resistance and powering. Biofouling 23, 331–341. doi:https://doi.org/10.1080/08927010701461974.
Schultz, M.P., Bendick, J.A., Holm, E.R., Hertel, W.M., 2011. Economic impact of biofouling on a naval surface ship. Biofouling 27, 87–98. doi:https://doi.org/10.1080/08927014.2010.542809.
Shih, T.H., Liou, W.W., Shabbir, A., Yang, Z., Zhu, J., 1995. A new $k-\epsilon$ eddy viscosity model for high reynolds number turbulent flows: Model development and validation. Comput. Fluids. 24, 227–238.
Smith, T., Jalkanen, J., Anderson, B., Corbett, J., Faber, J., Hanayama, S., O?Keeffe, E., Parker, S., Johansson, L., Aldous, L., Raucci, C., Traut, M., Ettinger, S., Nelissen, D., Lee, D., Ng, S., Agrawal, A., Winebrake, J., Hoen, M., Chesworth, S., Pandey, A., 2014. Third IMO GHG Study 2014: Executive Summary and Final Report. Technical Report. International Maritime Organization.
Smits, A.J., Wood, D.H., 1985. The response of turbulent boundary layers to sudden perturbations. Annu. Rev. Fluid Mech 17, 321–358.
Song, S., Demirel, Y., Atlar, M., 2019. An investigation into the effect of biofouling on the ship hydrodynamic characteristics using cfd. Ocean Engineering 175, 122–137. doi:https://doi.org/10.1016/j.oceaneng.2019.01.056.
Song, S., Demirel, Y., Atlar, M., 2020a. Penalty of hull and propeller fouling on ship self-propulsion performance. Applied Ocean Research doi:https://doi.org/10.1016/j.apor.2019.102006.
Song, S., Demirel, Y., Atlar, M., Shi, W., 2020b. Prediction of the fouling penalty on the tidal turbine performance and development of its mitigation measures. Applied Energy 276, 115498. doi:https://doi.org/10.1016/j.apenergy.2020.115498.
UNCTAD, 2017. Review of maritime transport, in: Proc. United Nations Conference on Trade and Development, Palais des Nations, 1211 Geneva 10, Switzerland.
Utama, I.K.A.P., Nugroho, B., 2018. Biofouling, ship drag, and fuel consumption: A brief overview. J. Ocean Tech. 13(2), 43–48.
Vanderwell, C., Ganapathisubramani, B., 2015. Effects of spanwise spacing on large-scale secondary flows in rough-wall turbulent boundary layers. J. Fluid Mech. 774, R2. doi:https://doi.org/10.1017/jfm.2015.292.
Versteeg, H., Malalasekera, W., 2007. An Introduction to Computational Fluid Dynamics: The Finite Volume Method. Longman Scientific, Harlow, UK.
Wangsawijaya, D., Baidya, R., Chung, D., Marusic, I., Hutchins, N., 2020. The effect of spanwise wavelength of surface heterogeneity on turbulent secondary flows. J. Fluid Mech. 894, A7.
Wangsawijaya, D.D., de Silva, C.M., Baidya, R., Chung, D., Marusic, I., Hutchins, N., 2018. Secondary flow over surfaces with spanwise heterogeneity, in: Proc. 21st Australasian Fluid Mech. Conf., Adelaide, Australia.
Wangsawijaya, D.D., de Silva, C.M., Baidya, R., Chung, D., Marusic, I., Hutchins, N., 2019. The instantaneous structure of turbulent boundary layers over surfaces with spanwise heterogeneity, in: Proc. 11th Turbulence and Shear Flow Phenomenon, Southampton, UK.
White, F.M., 2011. Fluid Mechanics. 7th ed., McGraw-Hill, New York. doi:https://doi.org/10.1016/B978-0-12-546801-5.50017-7.
Wood, D.H., 1982. Internal boundary layer growth following a step change in surface roughness. Boundary Layer Meteorology 22, 241–244.